THE HOST GALAXY AND CENTRAL ENGINE OF THE DWARF ACTIVE GALACTIC NUCLEUS POX 52[1,2]

Carol E. Thornton,[3] Aaron J. Barth,[3] Luis C. Ho,[4] Robert E. Rutledge,[5] and Jenny E. Greene[6,7]
Received 2008 May 16; accepted 2008 July 2

ABSTRACT

We present new multiwavelength observations of the dwarf Seyfert 1 galaxy POX 52 in order to investigate the properties of the host galaxy and the active nucleus and to examine the mass of its black hole, previously estimated to be $\sim 10^5 \, M_\odot$. *HST* ACS HRC images show that the host galaxy has a dwarf elliptical morphology ($M_I = -18.4$ mag, Sérsic index $n = 4.3$) with no detected disk component or spiral structure, confirming previous results from ground-based imaging. X-ray observations from both *Chandra* and *XMM-Newton* show strong (factor of 2) variability over timescales as short as 500 s, as well as a dramatic decrease in the absorbing column density over a 9 month period. We attribute this change to a partial covering absorber, with a 94% covering fraction and $N_{\rm H} = 58^{+8.4}_{-9.2} \times 10^{21}$ cm^{-2}, that moved out of the line of sight in between the *XMM-Newton* and *Chandra* observations. Combining these data with observations from the VLA, *Spitzer*, and archival data from 2MASS and *GALEX*, we examine the SED of the active nucleus. Its shape is broadly similar to typical radio-quiet quasar SEDs, despite the very low bolometric luminosity of $L_{\rm bol} = 1.3 \times 10^{43}$ ergs s^{-1}. Finally, we compare black hole mass estimators, including methods based on X-ray variability, and optical scaling relations using the broad Hβ line width and AGN continuum luminosity, finding a range of black hole mass from all methods to be $M_{\rm BH} = (2.2\text{–}4.2) \times 10^5 \, M_\odot$, with an Eddington ratio of $L_{\rm bol}/L_{\rm Edd} \approx 0.2\text{–}0.5$.

Subject headings: galaxies: active — galaxies: dwarf — galaxies: individual (POX 52) — galaxies: nuclei — galaxies: Seyfert — X-rays: galaxies

1. INTRODUCTION

Stellar dynamical and gasdynamical studies have proven to be the most secure method of measuring the masses of supermassive black holes in nearby galaxies, and black holes with masses of $\sim 10^6$–$10^9 \, M_\odot$ have now been detected in a few dozen galaxies (for a recent review see Ferrarese & Ford 2005). With just a few exceptions, however, stellar dynamical and gasdynamical techniques for black hole mass measurement cannot be applied to Seyfert galaxies and quasars because most luminous active galaxies are too distant for their black hole's gravitational sphere of influence to be resolved. Most black hole mass estimates in broad-lined active galactic nuclei (AGNs) are based on indirect methods that rely on scaling relations resulting from reverberation-mapping data (Kaspi et al. 2000; Bentz et al. 2006). Using these methods, it has recently become possible to search for active galaxies having extremely low mass black holes, in order to extend our understanding of black hole demographics to objects having black hole masses of $M_{\rm BH} \lesssim 10^6 \, M_\odot$.

The best nearby example of a black hole in the $< 10^6 \, M_\odot$ mass range is that in the dwarf Seyfert 1 galaxy NGC 4395 (Filippenko & Sargent 1989; Filippenko & Ho 2003). NGC 4395 is an essentially bulgeless, late-type dwarf galaxy with type 1 Seyfert

characteristics such as broad emission lines (Filippenko & Sargent 1989; Filippenko et al. 1993) and rapid X-ray variability (Iwasawa et al. 2000; Shih et al. 2003; Moran et al. 2005). Located at a distance of only ~ 4.3 Mpc (Thim et al. 2004), it is an excellent target for multiwavelength observations despite the tiny luminosity of its central engine ($L_{\rm bol} \approx 6 \times 10^{40}$ ergs s^{-1}; Moran et al. 1999). A recent ultraviolet (UV) reverberation-mapping measurement found $M_{\rm BH} = (3.6 \pm 1.1) \times 10^5 \, M_\odot$ (Peterson et al. 2005). Greene & Ho (2004, 2007b) searched the Sloan Digital Sky Survey (SDSS) archives to find AGNs with low-mass black holes and have found numerous examples of Seyfert 1 galaxies with $M_{\rm BH} < 10^6 \, M_\odot$, which we refer to as the GH sample. However, most of the SDSS objects found by Greene & Ho (2004, 2007b) are much more distant than NGC 4395, making detailed studies of their nuclei and host galaxies more difficult. Although the GH sample does contain examples of AGNs in low-mass disk galaxies (see also Dong et al. 2007), NGC 4395 remains an exceptional case due to its extreme late-type morphology, as well as its proximity.

POX 52, also known as G1200−2038 or PGC 038055 ($D = 93$ Mpc for $H_0 = 70$ km s^{-1} Mpc^{-1}), is an interesting counterpart to NGC 4395. It was originally discovered in an objective prism study by Kunth et al. (1987), who classified it as a dwarf disk galaxy with a Seyfert 2 nucleus, but noted the presence of a weak broad component of the Hβ line. Barth et al. (2004) reobserved POX 52, classifying it as a type 1 AGN based on clear detections of broad Hα and Hβ and noting that its optical emission line spectrum is nearly identical to that of NGC 4395. Both NGC 4395 and POX 52 can be classified as narrow-line Seyfert 1 (NLS1) galaxies, since they satisfy the defining criterion of having FWHM(Hβ) < 2000 km s^{-1}. NLS1 galaxies are often, but not always, characterized by strong Fe II emission and relatively weak [O III] emission when compared to Hβ along with steep soft (0.5–2.0 keV) spectral slopes and rapid variability in the X-ray (Osterbrock & Pogge 1985; Boller et al. 1996). NGC 4395 and POX 52 are therefore somewhat atypical NLS1

[3] Department of Physics and Astronomy, University of California, Irvine, CA 92619-4575; thorntoc@uci.edu, barth@uci.edu.

[4] The Observatories of the Carnegie Institution of Washington, Pasadena, CA 91101.

[5] Department of Physics, McGill University, Montreal, QC H3A 2T8, Canada.

[6] Department of Astrophysical Sciences, Princeton University, Princeton, NJ 08544.

[7] Hubble Fellow and Princeton-Carnegie Fellow.

galaxies in that they have very high excitation spectra with large [O III]/Hβ ratios and very weak Fe II emission.

Using the virial scaling relation calibrated by Kaspi et al. (2000), Barth et al. (2004) estimated a black hole mass of $M_{BH} \approx 1.6 \times 10^5 \, M_\odot$, making this one of the least massive black holes identified in any AGN. This mass is consistent with the mass expected based on the M_{BH}-σ_* relation (extrapolated to small σ_*) for the measured stellar velocity dispersion $\sigma_* = 36 \pm 5$ km s^{-1}. They also estimated the bolometric luminosity ($L_{bol} \approx 2 \times 10^{43}$ ergs s^{-1}) and the Eddington ratio ($L_{bol}/L_{Edd} \approx 0.5$–1) for POX 52. Thus, although POX 52 and NGC 4395 have very similar black hole masses and emission-line spectra that are nearly identical in appearance, the AGN in POX 52 is $\sim$300 times more luminous than that in NGC 4395, which has an estimated $L_{bol}/L_{Edd} \approx 10^{-3}$ (Peterson et al. 2005). Barth et al. (2004) used ground-based images to study the morphology of POX 52 and found that the host galaxy was best fitted with a Sérsic model with an index of $n = 3.6 \pm 0.2$, effective radius of $r_e = 1.2''$, and absolute magnitude $M_V = -17.6$. Combined with σ_* measured from the spectrum, these results show POX 52 to fall near the dwarf elliptical sequence (Geha et al. 2003) in the fundamental plane projections of Burstein et al. (1997), making it the first example of a dwarf elliptical to host a Seyfert nucleus. Although the past few years have seen a large increase in the number of known AGNs with low-mass black holes, POX 52 remains a valuable target for further study because of its relatively small distance and the fact that it is a less luminous and presumably less massive galaxy than the majority of the host galaxies in the GH SDSS sample.

Among nearby dwarf ellipticals, there is little evidence for the presence of central black holes. The closest well-studied example is NGC 205 in the Local Group, and stellar dynamical observations with the *Hubble Space Telescope* (*HST*) have set an upper limit to the black hole mass of $M_{BH} < 3.8 \times 10^4 \, M_\odot$ (Valluri et al. 2005), which is below the mass expected from a simple extrapolation of the M_{BH}-σ_* relation. For dwarf elliptical galaxies outside the Local Group, stellar dynamical observations lack the spatial resolution needed to detect black holes, and AGN surveys are the best available alternative for black hole searches. A double nucleus in one Virgo dwarf elliptical galaxy has been interpreted as morphological evidence for a stellar disk in orbit around a central black hole (Debattista et al. 2006), but aside from NGC 205 there are essentially no direct observational constraints on the black hole occupation fraction in dwarf elliptical galaxies. POX 52 represents a unique opportunity to study, in depth, the unambiguous presence of a low-mass central black hole in a nearby dwarf elliptical galaxy.

Here we present new multiwavelength observations of POX 52, including the first targeted *HST* and X-ray observations of this unusual object. *HST* images are used to examine the host galaxy morphology; our results confirm the previous conclusions that the galaxy is consistent with a dwarf elliptical morphology with a Sérsic index of $\sim$4. We describe X-ray observations obtained with both the *Chandra* and *XMM-Newton* X-ray observatories in order to study the temporal and spectral properties of the active nucleus and to constrain its bolometric luminosity and black hole mass. We also include observations from the Very Large Array (VLA) and *Spitzer* Infrared Spectrometer (IRS), as well as archival data from the Two Micron All Sky Survey (2MASS) and *GALEX*, in order to investigate the spectral energy distribution (SED) of POX 52 over a wide range in frequency. We use recently updated versions of the broad-line virial scaling relations to obtain new estimates of the mass of the black hole, and in combination with the multiwavelength SED we determine the bolometric luminosity

and Eddington ratio for the AGN. In addition to the *HST* data presented here, we were also awarded time as part of the same project to obtain ultraviolet and optical spectra of POX 52 with the Space Telescope Imaging Spectrograph (STIS), but STIS failed before the observations were scheduled to be taken.

2. OPTICAL OBSERVATIONS

Observations of POX 52 were made on 2004 November 18 UT with *HST* using the High Resolution Camera (HRC) on the Advanced Camera for Surveys (ACS). Four images of 590 s each were taken through the F814W (*I* band; data sets J8YB10PQQ, J8YB10010) filter, and four images of 622 s each were taken through the F435W (*B* band; data sets J8YB10PVQ, J8YB10020) filter. These images were dithered using a four-point box pattern with 0.15″ spacing to enable the removal of cosmic-ray hits and bad pixels. An additional 100 s image was taken in each filter in the event that the nucleus saturated in the longer exposures, although this saturation did not occur in any image. The images for each filter were combined using the `multidrizzle` task in PyRAF (ver. 1.3) to remove cosmic-ray hits and to correct for the ACS geometric distortion, and the output images were not sky subtracted or rotated during this processing. These *HST* images (Fig. 1) show POX 52 as a bright point source centered in a smooth host galaxy with no obvious signs of spiral structure in either filter.

The two-dimensional fitting program GALFIT (ver. 2.1d; Peng et al. 2002) was used to model the host galaxy morphology. The central point source in the center of the host galaxy was modeled by a point-spread function (PSF) image, and the host galaxy itself was modeled by a Sérsic component or combination of Sérsic components. Since the sky background was not subtracted in the image processing, a sky component was also used within each galaxy model. All magnitudes are in the Vegamag system calculated using the zero points calibrated for HRC,[8] which are 25.188 for F435W and 24.861 for F814W, and corrected for Galactic extinction using the IRAF package SYNPHOT for $E(B - V) = 0.052$ mag (Schlegel et al. 1998).

2.1. PSF Modeling

The PSF image used in the GALFIT modeling can be either created synthetically from a program such as Tiny Tim (Krist 1993) or cropped from a data image using the same detector and filter set as the object being modeled. Both methods were tested in order to determine the most appropriate PSF for our analysis. We began by creating a synthetic PSF for each filter using Tiny Tim. We centered the PSF in the same position as the point source in our galaxy images in order to properly reproduce the geometric changes involved in the `multidrizzle` process. These PSF images were then `multidrizzled` in the same manner as the object data, since the Tiny Tim PSFs created for HRC include the geometric distortions in raw HRC images and therefore must be subject to the same corrections to undistort the images. In order to evaluate how well the Tiny Tim PSF compares to the PSF of a star observed with HRC, we searched the archive for unsaturated images of *HST* standard stars observed in the F814W and F435W filters, finding three that matched our criteria: G191-B2B, GD 153, and GD 71. Table 1 lists the observation dates and exposure times of these three white dwarf stars, in which they were located near the center of the CCD. The specific observations were chosen to bracket the POX 52 observation in order to minimize any changes to the PSF over time, with the average observation

---

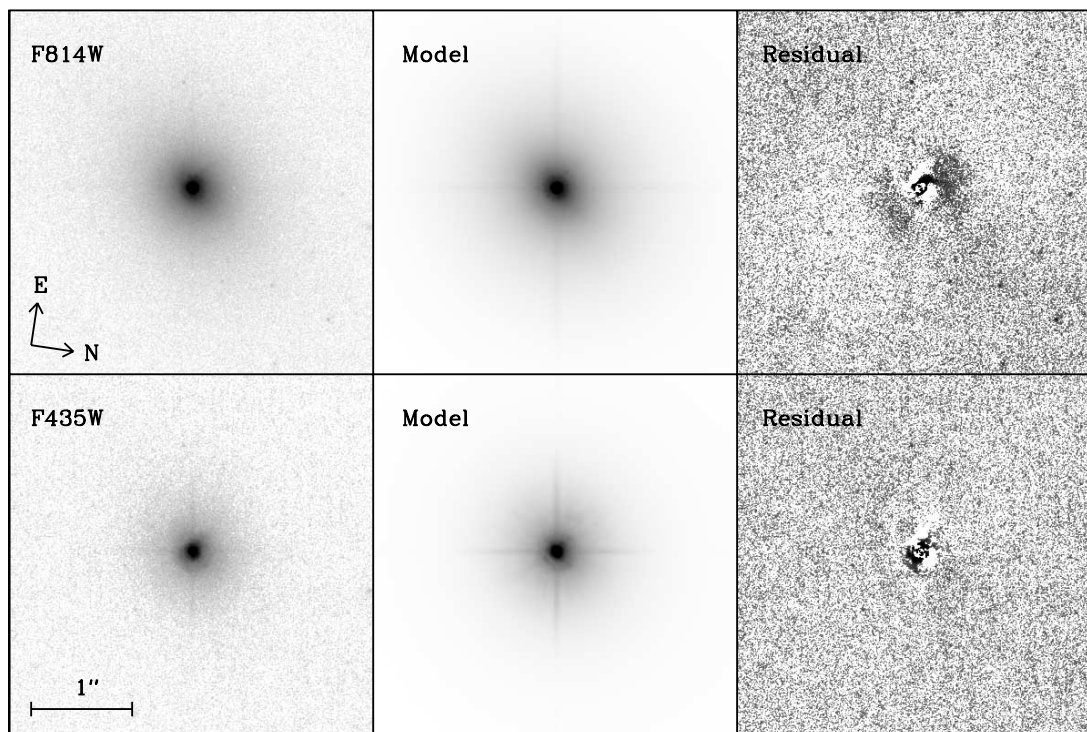[8] See http://www.stsci.edu/hst/acs/analysis/zeropoints.

Fig. 1.—*HST* ACS HRC images of POX 52 and GALFIT models. The top and bottom rows show the F814W and F435W images, respectively. In each row, the left panel is the ACS image, the middle panel is the full GALFIT model, and the right panel shows the fit residuals. For the F435W filter, the double-Sérsic host galaxy model is shown.

occurring 6 months from that of POX 52. All of the PSF star images were processed through `multidrizzle` in the same manner as our POX 52 data with the exception that the standard-star images were sky subtracted during the `multidrizzle` process in order to be used as input PSF images with GALFIT.

In order to determine how well Tiny Tim models the stellar PSF, we used the Tiny Tim model as the input PSF in GALFIT and fitted each of the standard stars in both of the observed filters. Not only can we examine how the shape of the PSF changes for different stars (due to color and/or CCD location), but the existence of multiple observations of each of these stars in the *HST* archive allows us to determine the extent of changes to the PSF over time. Figure 2 shows radial profile plots made using the IRAF task `ellipse` for the star images compared to the GALFIT model using the Tiny Tim PSFs. The three left panels are profiles from the three different stars found in the *HST* archive. One can see how the shape of the PSF's central peak can vary depending on the star used. The two observations of GD 71 were taken about a year and a half apart. There is not a large change in the PSF shape during this time period, but small differences are apparent. The

differences in profile shapes are more apparent in the F435W filter, showing that Tiny Tim has more difficulty modeling a PSF in this filter. The Tiny Tim F435W PSF tends to have a flatter inner core, leaving a ~0.3 mag arcsec^{-2} residual out to $\sim0.05''$. In the ACS HRC about 10%–20% of the PSF flux at long wavelengths ($\lambda > 7500$ Å) scatters into a halo surrounding the PSF core, making PSF modeling more difficult in red passbands (Sirianni et al. 1998), such as the F814W filter. The halo radius increases with wavelength, and Tiny Tim attempts to model its wavelength-dependent structure. Despite the red halo (seen as the bump at $\sim0.3''$ in Fig. 2) and the variations seen between the stellar PSFs, Tiny Tim did a reasonable job modeling each of the standard stars in the F814W filter, with few significant deviations between the shape of the Tiny Tim PSF and that of the observed star. Since the Tiny Tim PSFs reasonably fit the central regions of the observed stars in both filters and have the advantage of being noise-free, we selected the corresponding Tiny Tim PSF to use in the GALFIT modeling of POX 52.

2.2. *AGN and Host Galaxy Modeling*

We fit the F814W HRC image of POX 52 over a ~169 arcsec^2 (491×491 pixel) region with a simple model consisting of an AGN point source and a single Sérsic component, where all parameters (including position and magnitude for both the point-source and Sérsic components and effective radius, Sérsic index, axis ratio, and position angle for the Sérsic component) were allowed to vary. Figure 3 shows a radial profile plot of the best fit from GALFIT with a Sérsic index of 4.3 and a reduced χ^2 of 15.0 for 241,068 degrees of freedom (dof). The top panels of Figure 1 show the F814W *HST* image (*left panel*) and the GALFIT model (*middle panel*) with $m_{AGN} = 17.5$, $m_{host} = 16.2$, and an effective radius of $1.08''$, or 490 pc. The residuals after subtracting the model from the galaxy image are shown in the right panel. The strong residuals in the center of the image are

TABLE 1
STELLAR PSF OBSERVATIONS

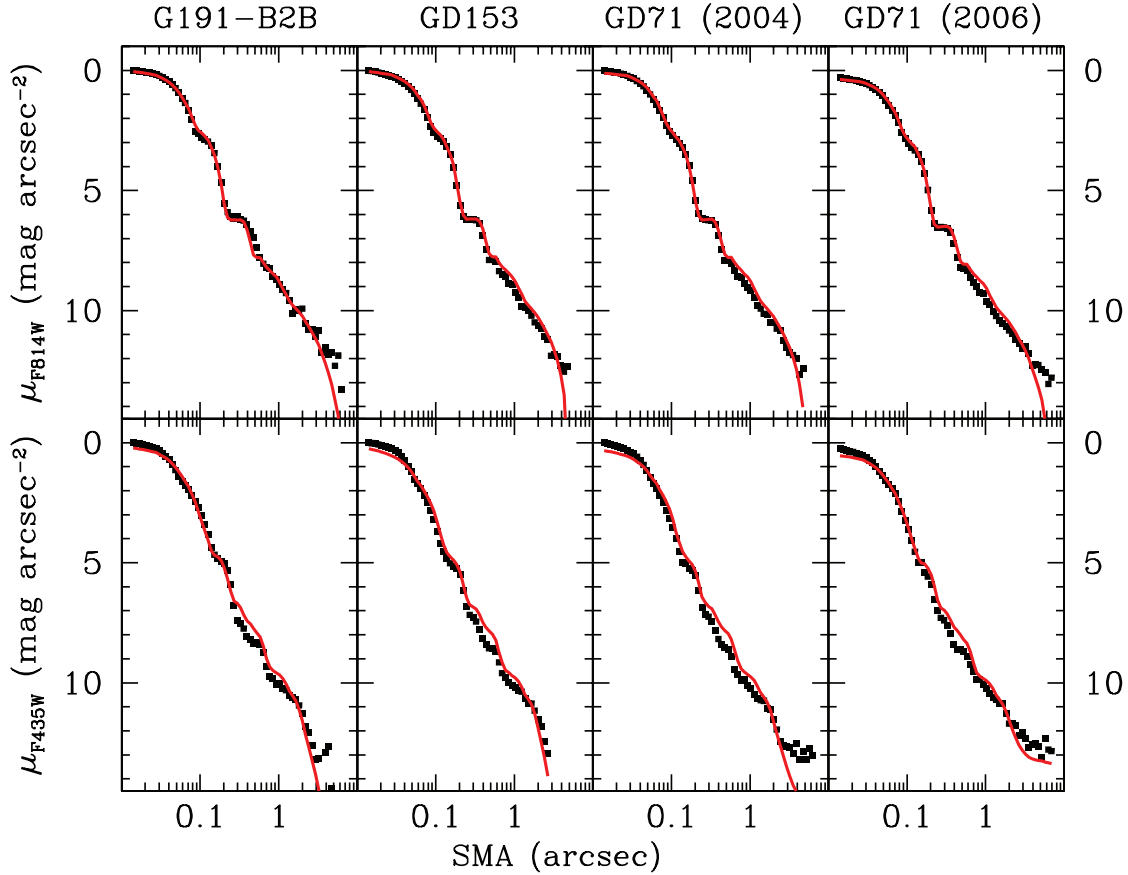| STAR	V (mag)	OBSERVATION DATE (UT)	EXPOSURE TIME (s)	
			F435W	F814W
G191-B2B	11.78	2003 Aug 30	3.2	4.0
	11.78	2003 Nov 8	4.0	14.0
	11.78	2005 Feb 28	4.0	10.0
GD 153	13.40	2004 Feb 15	14.4	40.0
	13.40	2005 May 19	14.4	30.0
GD 71	13.06	2004 Feb 3	12.0	35.0
	13.06	2006 Nov 20	11.0	26.0

Fig. 2.—Radial profile plots of the ACS HRC standard-star images along the semimajor axis (SMA), with the Tiny Tim synthetic PSFs overplotted in red. The magnitude scale is normalized to 0 mag arcsec^{-2} in the PSF core (except for the 2006 observation of GD 71, which uses the same offset as the 2004 observation in order to demonstrate time variability of the PSF structure). The bump at $\sim 0.4''$ in the F814W radial profiles is the long-wavelength scattering halo in ACS HRC.

mostly confined to the PSF-dominated region at $r < 0.1''$ and are likely to be the result of PSF mismatch, but the weaker residuals seen farther out from the PSF-dominated region of the galaxy could indicate small-scale structure in the host galaxy. We added a second Sérsic component to the model in an attempt to minimize the residuals, but it made little difference in the overall fit. The additional Sérsic component closely followed that of the PSF component, leaving the original Sérsic component to trace the host galaxy as before. The relative gain in the overall fit did not justify the need for a two Sérsic component model; therefore, we select the PSF+Sérsic model as the best fit to the F814W images. Parameters for this fit and the F435W fits can be seen in Table 2.

The F435W data proved to be more difficult to model. The galaxy image was initially fitted using the simple PSF+Sérsic model as above (Fig. 4, *left panel*), but this resulted in an unexpectedly high Sérsic index of $n = 20$ (the default maximum value for the Sérsic index used by GALFIT) and a poor fit compared with the F814W model results. In order to get a more reasonable result, we added a second Sérsic component to the model, allowing the parameters for both components to vary freely. In the resulting model fit, the first Sérsic component has a high central surface brightness that traces the central region of the galaxy out to $\sim 0.25''$, resembling the PSF component but with a slightly broader profile, while the second Sérsic component has a much lower surface brightness that models the majority of the host galaxy from $\sim 0.5''$ outward. This outermost Sérsic component has an index of $n = 4.4$, similar to the result of the F814W fit.

The effective radius of the host galaxy, as described by the outer Sérsic component in the best-fit (PSF+Sérsic+Sérsic) model, is slightly larger than in the F814W filter with $r_e = 1.22'' = 550$ pc. The reduced χ^2 is also larger than in the F814W filter (26.2 compared to 15.0, even including the second Sérsic component in the F435W model), and the PSF component has an unexpectedly low central surface brightness, as seen in the radial profile plot (Fig. 4, *right panel*).

The inner Sérsic component consists of some combination of AGN and host galaxy light, and it is difficult to disentangle the relative contributions. The magnitude of the PSF component describes a lower limit to the magnitude of the AGN of $m_{\rm AGN} = 19.2$. We estimate an upper limit by repeatedly fitting the galaxy with a PSF+Sérsic model with a fixed PSF magnitude, increasing the magnitude each time until it was bright enough to account for the majority of the light in the very center of the galaxy, while allowing the single Sérsic component to vary freely as before. This results in an AGN magnitude of $m_{\rm AGN} = 18.6$, which puts the AGN magnitude in the F435W filter in the range of $m_{\rm AGN} = 18.6–19.2$ mag. We adopt the magnitude of the outermost Sérsic component as a lower limit to the host galaxy brightness, $m_{\rm host} = 18.2$, in the F435W filter and combine the magnitudes of both Sérsic components to determine the upper limit, $m_{\rm host} = 17.5$. This results in a host galaxy magnitude range of $m_{\rm host} = 17.5–18.2$ mag.

In order to further confirm our choice of PSF, we refit the galaxy images with both the PSF+Sérsic model and the PSF+Sérsic+Sérsic model using each of the stellar PSFs. In each of the fits, regardless of the star used or the filter the image was taken in, the PSF component drastically underrepresented the central point-source light contribution. This verified that the
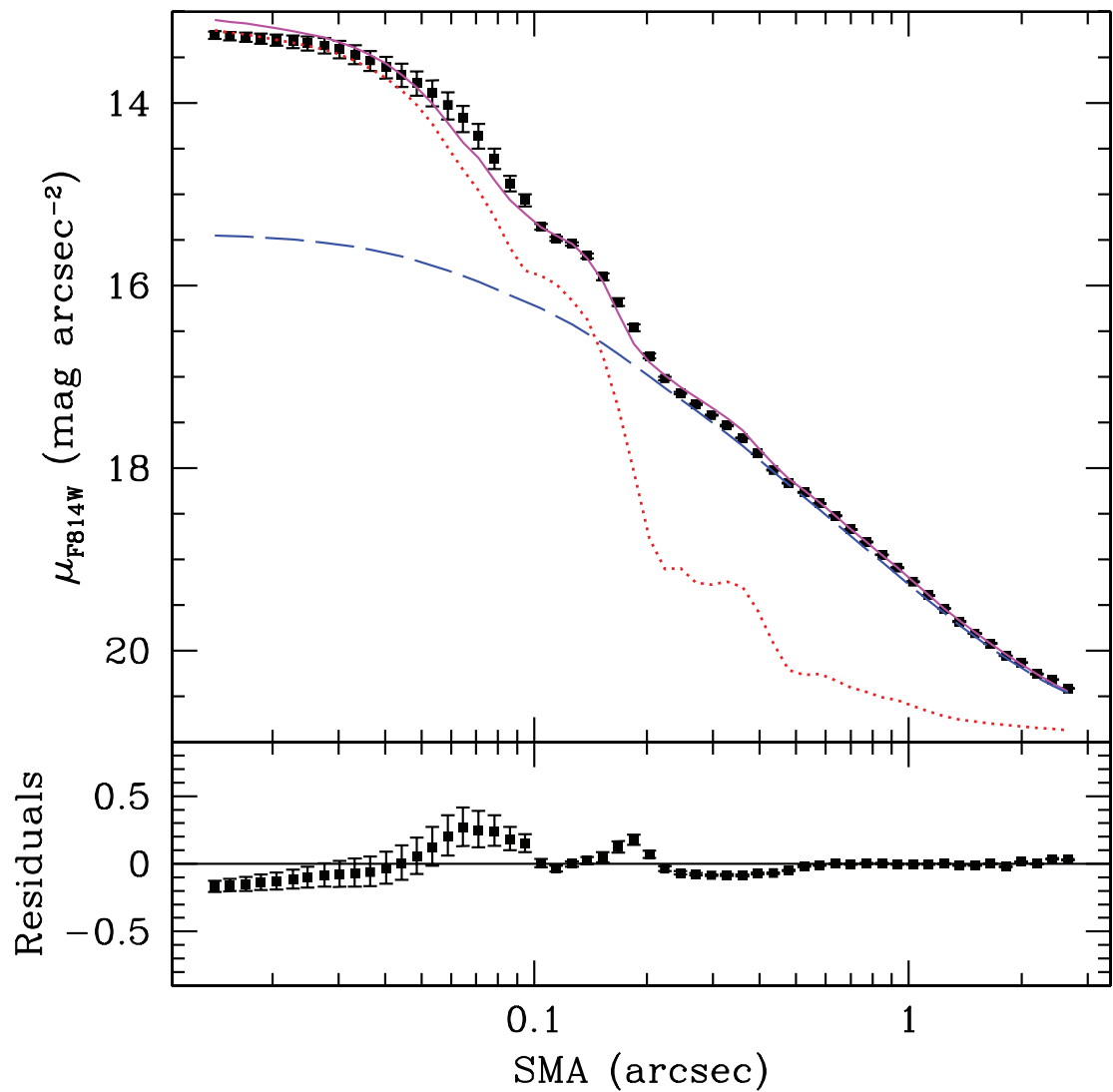
Fig. 3.—Radial profile plot of the surface brightness (*top*) of POX 52 in the F814W filter with residuals (*bottom*) between the data and the total fit. The black squares are the data, the solid magenta line is the total fit from GALFIT, the dotted red line is the PSF component, and the dashed blue line is the Sérsic component.

fits in which the noise-free Tiny Tim PSF was used produced the best overall results.

Our GALFIT results show that the host galaxy of POX 52 has a Sérsic index $n \approx 4$ in both the F814W and F435W filters, making it more centrally concentrated than a typical dwarf elliptical galaxy with $n \approx 0.3$–3 (Binggeli & Jerjen 1998). In a study of host galaxies containing similar low-mass AGNs, Greene et al. (2008) selected 19 galaxies from the GH sample for *HST* imaging in order to better determine their host galaxy morphology. From

this *HST* imaging, they find that 60% of the members of the sample are disk-dominated galaxies, while the remainder are compact systems with host morphology similar to POX 52. These compact galaxies have steep Sérsic indices in the range of 2–4 and reside near dwarf ellipticals from the Geha et al. (2002), Gavazzi et al. (2005), and Matković & Guzmán (2005) samples in the fundamental plane. Although many of the galaxies in the Greene et al. (2008) *HST* sample are quite similar to POX 52 in terms of Sérsic index and overall host galaxy morphology,

TABLE 2
GALFIT Results

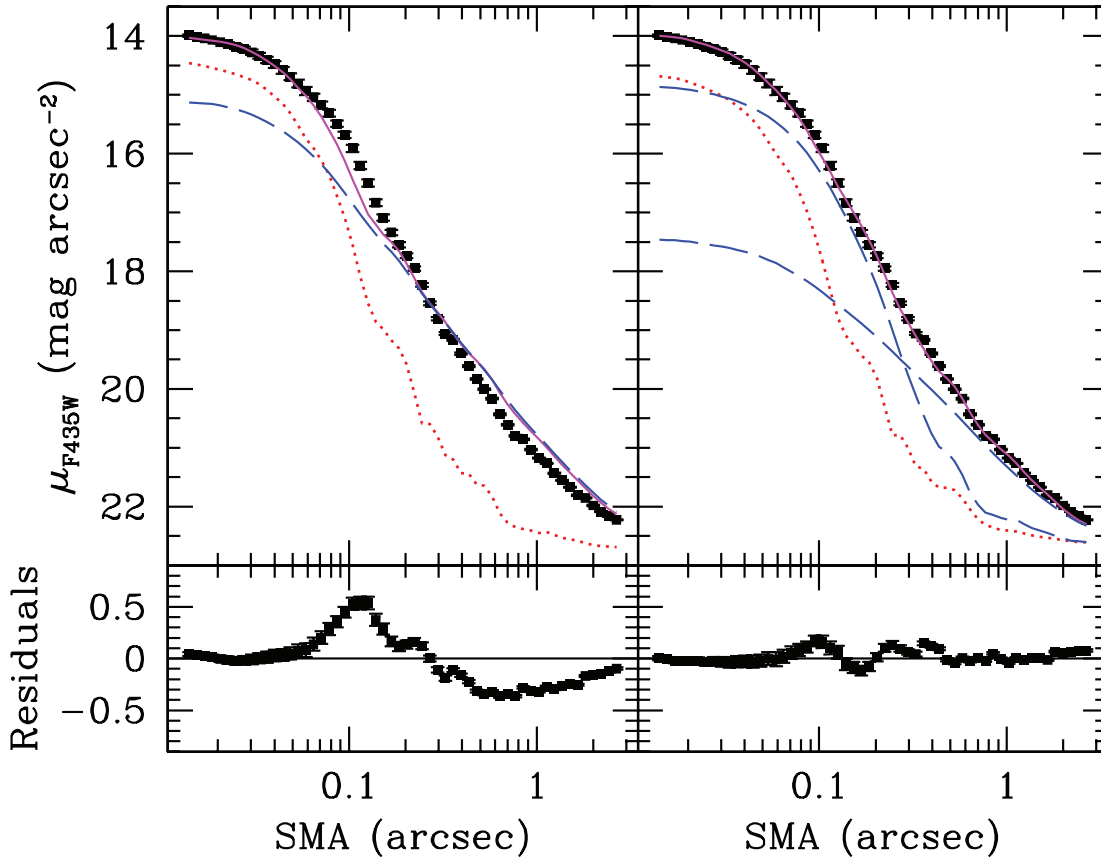| Band	χ^2/ν	Component	Magnitude	n	r_e (arcsec pc^{-1})
F814W..................................	15.0	PSF	17.5	. . .	. . .
	15.0	Sérsic	16.2	4.3	1.08/490
F435W: single Sérsic.............	31.6	PSF	19.0	. . .	. . .
	31.6	Sérsic	16.8	20.0	5.87/2700
F435W: double Sérsic	26.2	PSF	19.2	. . .	. . .
	26.2	Sérsic 1	18.4	1.4	0.060/27
	26.2	Sérsic 2	18.2	4.4	1.22/550

Fig. 4.—Radial profile plots of the surface brightness (*top panels*) of POX 52 in the F435W filter with residuals (*bottom panels*) between the data and the total fit. The black squares are the data, the solid magenta lines are the total fits from GALFIT, the dotted red lines are the PSF components, and the dashed blue lines are Sérsic components. *Left*: Best-fit GALFIT model using only one Sérsic component. *Right*: Best-fit GALFIT model using two Sérsic components.

POX 52 ($M_{host} = -18.4$ in the F435W filter) remains less luminous than the average galaxy in the GH sample by ~ 2 mag (Greene et al. 2008).

3. X-RAY OBSERVATIONS

3.1. *Chandra*

We first describe the *Chandra* observation since the source exhibited less spectral complexity in the *Chandra* data than in the earlier *XMM-Newton* observation. X-ray observations of POX 52 (dataset obs/5736) were carried out using the Advanced CCD Imaging Spectrometer (ACIS) instrument on the *Chandra X-Ray Observatory* for a total of 25 ks on 2006 April 18 UT. The level 2 event file was restricted to the 0.5–10.0 keV energy range, and there were no periods of high background found. POX 52 was observed to be consistent with a point-source object, such that the FWHM of the PSF was $\sim 0.5''$, the 70% and 90% encircled energy radii were ~ 1.5 and 2 pixels, respectively,[9] and the source showed no extended emission (Fig. 5). Source events were extracted using a circular region of radius 10 pixels (4.9'') centered on POX 52. The source was too close to the edge of the CCD to use an annulus as the background region; therefore, a circular background region was extracted 46'' away on the same chip with a radius of 24.6''. There were approximately 1.2×10^{-6} counts s^{-1} pixel^{-2} within this background region, giving a background-subtracted average source count rate of 0.20 counts s^{-1}. Due to the low source count rate, pileup was not an issue. Data were analyzed using standard tasks, such as `dmextract` and

[9] This is consistent with *Chandra* PSF analysis. For more information, see http://cxc.harvard.edu/proposer/POG/html/ACIS.html#tth_sEc6.6.

`psextract` in CIAO (ver. 3.4/4.0β1; CALDB, ver. 3.4.0) and spectral models in XSPEC (ver. 12.3.0t).

All light curves were created using time bins of 500 s and split into 0.5–10.0, 0.5–1.0, and 1.0–10.0 keV energy ranges. These are denoted as the "full," "soft," and "hard" bands, respectively.
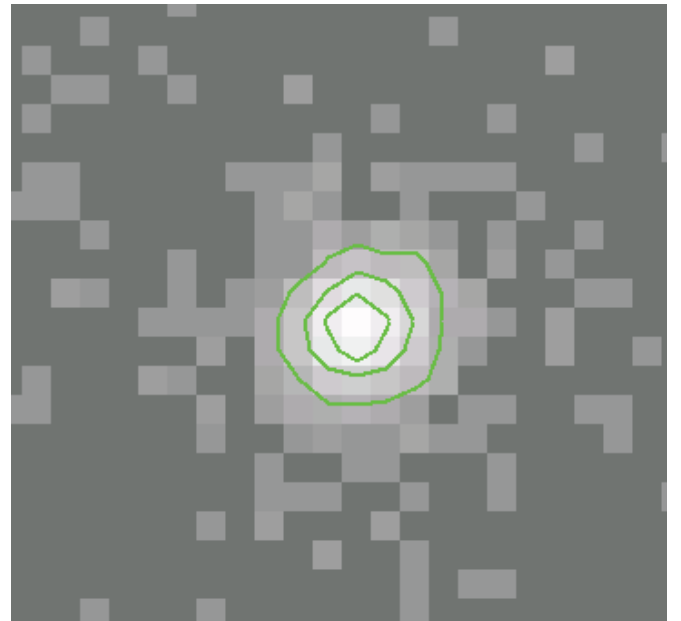

Fig. 5.—*Chandra* image of POX 52 with intensity (68%, 90%, and 99%) contours overlaid. Image is 11'' on a side.
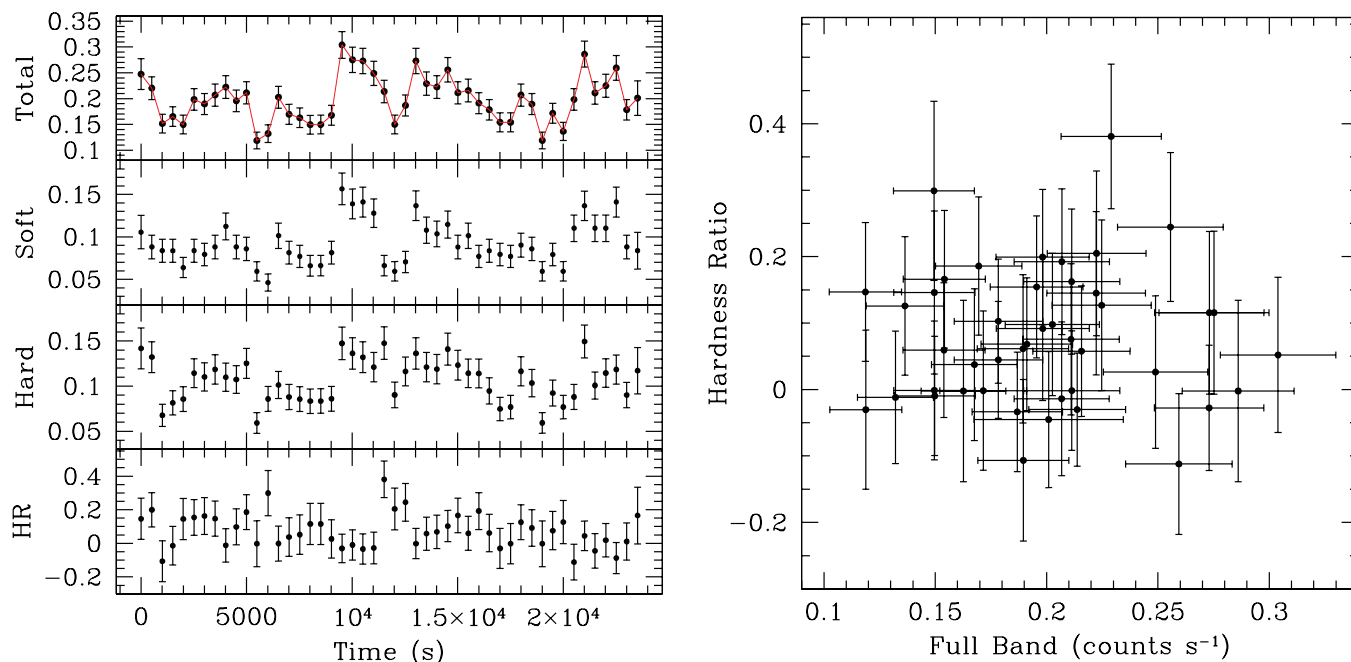
FIG. 6.—*Left*: Light curves of POX 52 taken from *Chandra* data. The top panel is the full (0.5–10.0 keV) light curve in counts s^{-1}, the second panel is the soft (0.5–1.0 keV) X-ray light curve, the third panel is the hard (1.0–10.0 keV) X-ray light curve, and the bottom panel is the hardness ratio (HR). *Right*: Plot of hardness ratio vs. the count rate in the full band.

The full-band light curve (Fig. 6, *top panel*) shows strong (factor of 2) variability over short (∼500 s) timescales. Also shown in Figure 6 are the light curves for the soft band, hard band, and the hardness ratio, HR = (hard − soft)/(hard + soft). There seems to be no significant correlation between hardness ratio and the flux from the full band as seen in the right panel of Figure 6, and this is confirmed by the results of a Spearman rank correlation test. The correlation coefficient was −0.16, which describes a weak anticorrelation, with a significance of 0.27 that is essentially insignificant.

The ACIS spectrum was first fitted over the range 0.5–10.0 keV with a simple absorbed power law, allowing all parameters to vary freely and optimized using the Cash (1979) *C* statistic rather than χ^2. The *C* statistic is a better goodness-of-fit parameter when fitting low signal-to-noise ratio spectra. The absorbed power law poorly fitted the soft end of the observed spectrum, requiring another component to help model the excess of soft energies properly. We added a disk blackbody component to the model (phabs*[powerlaw+diskbb]), which resulted in an acceptable fit to the observed X-ray spectrum (Fig. 7). The
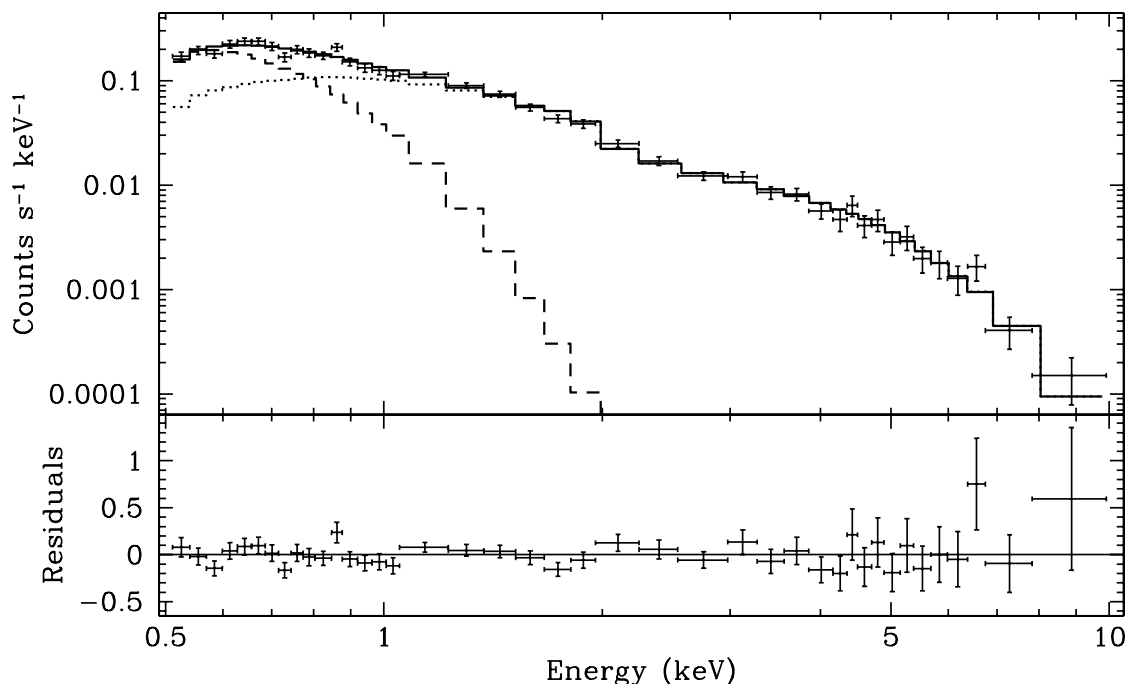

FIG. 7.—*Chandra* spectrum from 0.5 to 10.0 keV modeled (*thick line*) with an absorbed power law (*dotted line*) and disk blackbody (*dashed line*). Residuals are calculated as residual = (data − model)/model.
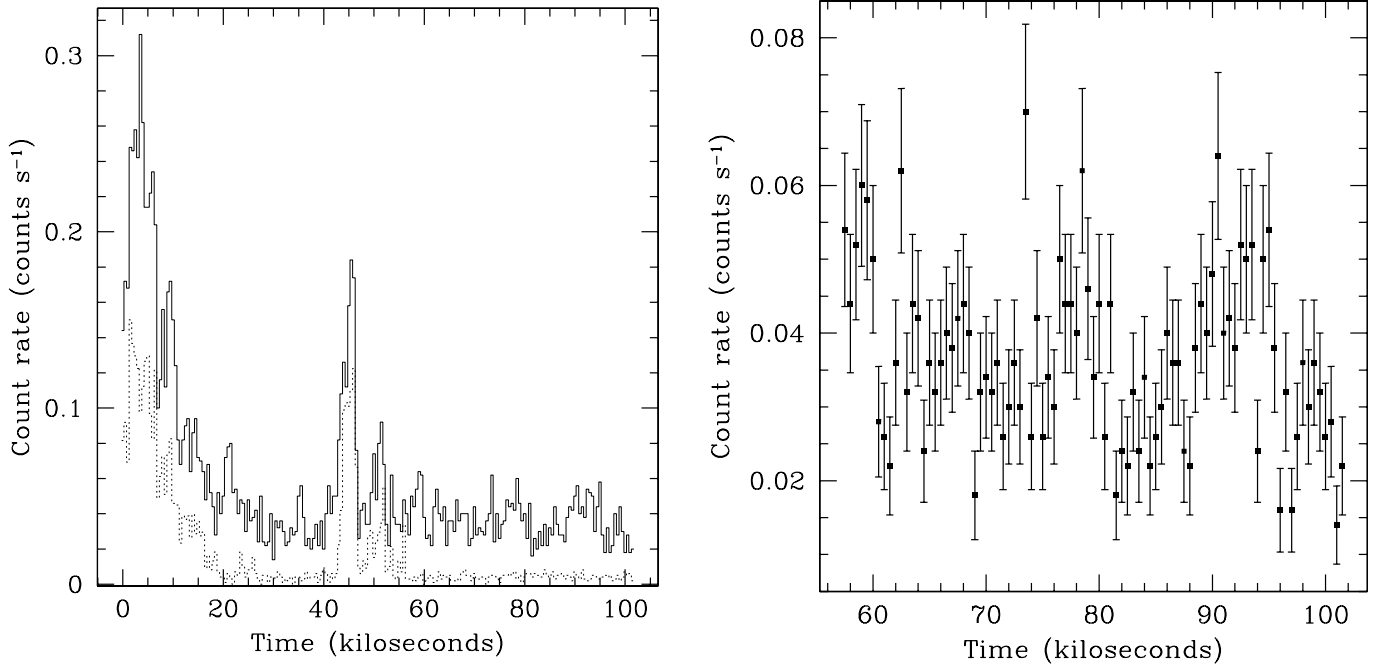
Fig. 8.—*Left*: *XMM-Newton* EPIC pn light curve (*solid line*) from 0.5 to 10.0 keV over the full 100 ks observation. The background spectrum is the dotted line. Note the large background flares at 0–10 ks and 40–55 ks. *Right*: Background-subtracted light curve of the second half of the observation starting at 57.5 ks, used in the spectral fit.

best-fitting model had a photon index of $\Gamma = 1.8 \pm 0.15$ and a disk blackbody temperature of $T_{BB} = 0.13^{+0.03}_{-0.02}$ keV. The absorbing column density was $N_H = 0.50^{+1.1}_{-0.01} \times 10^{21}$ cm^{-2}, only slightly in excess of the predicted foreground column of $N_H \approx 0.4 \times 10^{21}$ cm^{-2} based on Galactic H I maps (Dickey & Lockman 1990; Kalberla et al. 2005), as determined by the HEASARC online N_H calculator.[10]

In place of the thermal disk blackbody, we tested fitting the spectrum with other thermal components plus the absorbed power-law component, specifically the thermal bremsstrahlung model and the Raymond-Smith (Raymond & Smith 1977) plasma model. The bremsstrahlung model, with all parameters allowed to vary freely, produced a poor fit that strongly underpredicted the soft X-ray end of the spectrum by $\sim$3 orders of magnitude. The Raymond-Smith model produced a reasonable fit to the data, similar to the fit when the disk blackbody was used, with a C statistic of 182, nearly identical to the result for the combined absorbed power-law and disk blackbody model ($C = 183$). However, this model uses four free parameters (three when the redshift is frozen) to fit the data, compared to the two parameters used in the disk blackbody model. Due to this difference, we select the combined absorbed power law and disk blackbody as our best-fit model for simplicity.

There is possible evidence for an Fe K emission line seen in a single bin of energy $E = 6.6$ keV in the residuals of our best-fit model. We added a Gaussian component to our model in order to determine constraints on the line energy and width. Allowing both the line energy and line width to vary freely, but fixing all other model parameters to our previous best-fit values, XSPEC modeled the line centroid at $6.71^{+0.07}_{-0.12}$ keV with a line width ranging from $\sigma_{line} = 0$ to 0.82 keV and an equivalent width (EW) of $0.3^{+0.9}_{-0.3}$ keV. The large EW may be explained by the X-ray Baldwin effect (see Page et al. 2004; Jiang et al. 2007), but we cannot draw any firm conclusions, since the detection is

marginal, at best. Nandra et al. (2007) analyzed *XMM-Newton* spectra of 26 Seyfert galaxies (mostly Seyfert 1) and compiled measurements of the Fe Kα line. In this sample, the Fe Kα energies ranged from 5.28 to 6.78 keV, with a range of equivalent widths of 0.009–0.394 keV. Both the measured line energy and EW of the Fe Kα from POX 52 are within the range of values measured by Nandra et al. (2007), although the EW is at the high end of the values sampled. The large errors on these measurements make this a weak detection at best, and deeper observations are needed to obtain a definitive detection of the line.

3.2. *XMM-Newton*

XMM-Newton observed POX 52 on 2005 July 8–9 UT for a total exposure time of 100 ks on each of the three EPIC instruments: pn, MOS1, and MOS2. All data were reduced using the Science Analysis System (SAS, ver. 7.0.0) and XSPEC following the guidelines of the SAS Cookbook and SAS ABC-Guide. For all EPIC instruments, the source was extracted in a circular region with a radius of 32″, and due to the proximity of the source to the edge of the CCD in the EPIC pn camera, the background was extracted from a circular region free of sources, located 107″ away from the source with a radius of 44.9″. Only events corresponding to patterns 0–4 (single or double pixel events) were used for the pn event file and patterns 0–12 (single, double, triple, and quadruple pixel events) for the MOS event files. All event files were restricted to an energy range of 0.5–10.0 keV to better compare with the *Chandra* data. For all three instruments, events were excluded that occurred next to the edges of the CCD or next to bad pixels. Again, the source count rate was low enough to neglect effects due to pileup.

Again using 500 s time bins, a light curve (Fig. 8) was created using the entirety of the pn data set. However, the first half of the observation contained two large background flares, and due to this contamination, only the second half of the observation (Fig. 8, *right panel*) was used in the spectral analysis (where the total counts in the background region are $\sim$11.5% of the source counts).

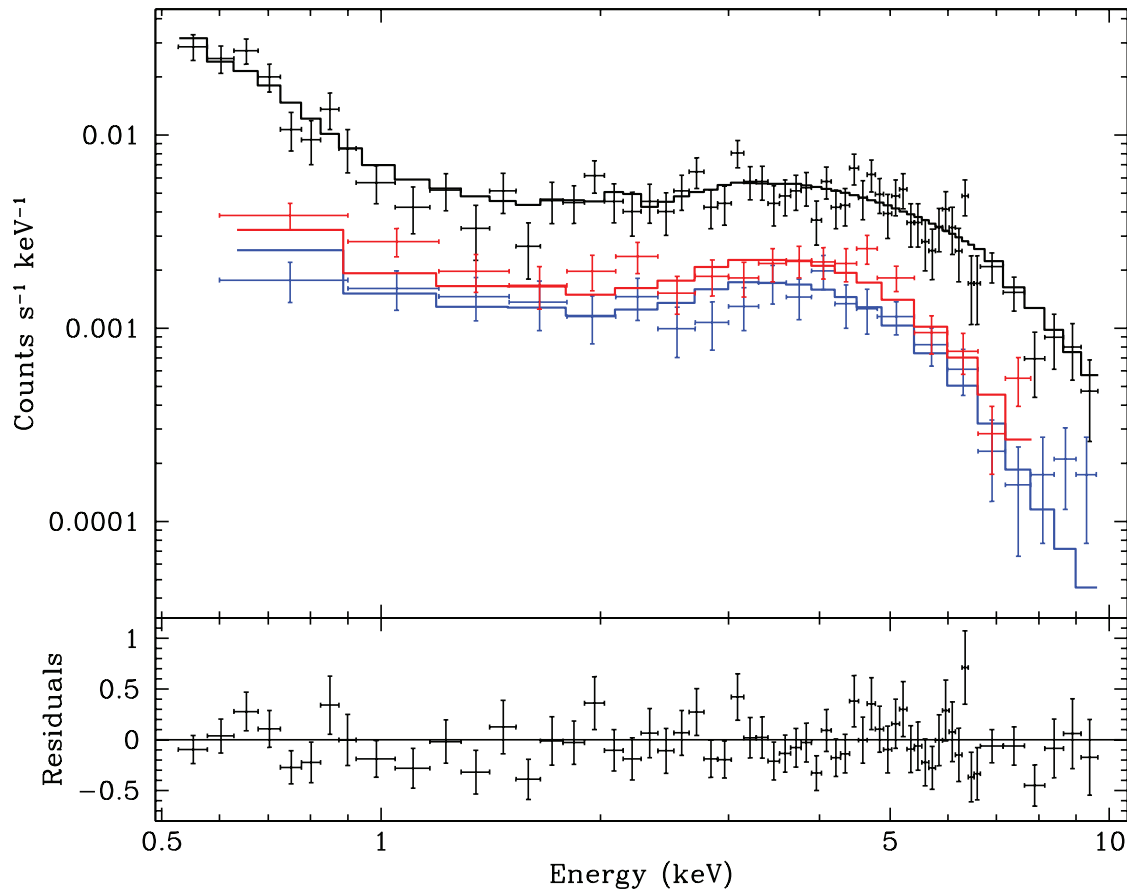[10] See http://heasarc.gsfc.nasa.gov/cgi-bin/Tools/w3nh/w3nh.pl.

Fig. 9.—*XMM-Newton* spectra over 0.5–10.0 keV, modeled with an absorbed power law, disk blackbody, and a partial covering model with all parameters allowed to vary freely. The pn data are in black, MOS 1 data are in blue, and MOS 2 data are in red. The corresponding models are shown as solid lines in their respective colors. The bottom panel shows the residuals (calculated as residual = [data − model]/model) for the EPIC pn data.

Examination of the second half of the observation shows a similar amplitude of variability to the *Chandra* observations, but over slightly longer (10^3–10^4 s) timescales.

Observations of POX 52 with *XMM-Newton* yielded a significantly lower flux than the subsequent *Chandra* data. Figure 9 shows the spectra from both the pn and MOS cameras. There is a hint of a detection of a narrow Fe K emission line near 6.4 keV (contained in the bin centered at 6.375 keV with a width of 0.125 keV), as can be seen in the EPIC pn residuals (Fig. 9, *bottom panel*). A simple absorbed power law and a combined absorbed power law plus disk blackbody both proved to be poor fits, even when the same parameter values were used

from the *Chandra* fit, underpredicting the spectral shape by 1–2 orders of magnitude below ~1 keV.

The *XMM-Newton* spectrum is harder than in the *Chandra* observation and requires more absorption to fit the spectral shape. Adding a partial covering component to the model (phabs*pcfabs*[powerlaw+diskbb]) improved the fit significantly. We fit the data using this model, allowing all parameters to vary freely. The photon index and blackbody temperature of this model are consistent within the errors with values derived from the *Chandra* data. Parameters for the *Chandra* and *XMM-Newton* best-fit models are in Table 3. The major difference is the need for much higher levels of absorption. The absorbing

TABLE 3
X-Ray Spectral Properties

Parameter	*Chandra*	*XMM-Newton*
C statistic	183 (210 PHA bins, 205 dof)	111 (104 PHA bins, 97 dof)
Photon index Γ	1.8 ± 0.15	$1.8^{+0.26}_{-0.24}$
Disk T_{BB} (keV)	$0.13^{+0.03}_{-0.02}$	$0.09^{+0.03}_{-0.01}$
Foreground N_H (10^{21} cm^{-2})	$0.50^{+1.1}_{-0.01}$	$1.61^{+2.6}_{-1.2}$
Partial covering N_H (10^{21} cm^{-2})	...	$58^{+8.4}_{-9.2}$
Partial covering fraction (%)	...	$94^{+2.2}_{-3.3}$
$F(0.5$–10 keV) (10^{-13} ergs cm^{-2} s^{-1})	$12.6^{+0.05}_{-2.7}$	$3.2^{+0.42}_{-1.51}$
$L(0.5$–10 keV) (10^{42} ergs s^{-1})	$1.50^{+0.01}_{-0.37}$	$1.38^{+0.19}_{-0.82}$

Notes.—All model parameters were fitted over a 0.5–10.0 keV energy range, and we present observed flux and unabsorbed luminosity for both observations. For *XMM-Newton*, the spectra from both the EPIC pn and MOS cameras were fitted simultaneously.
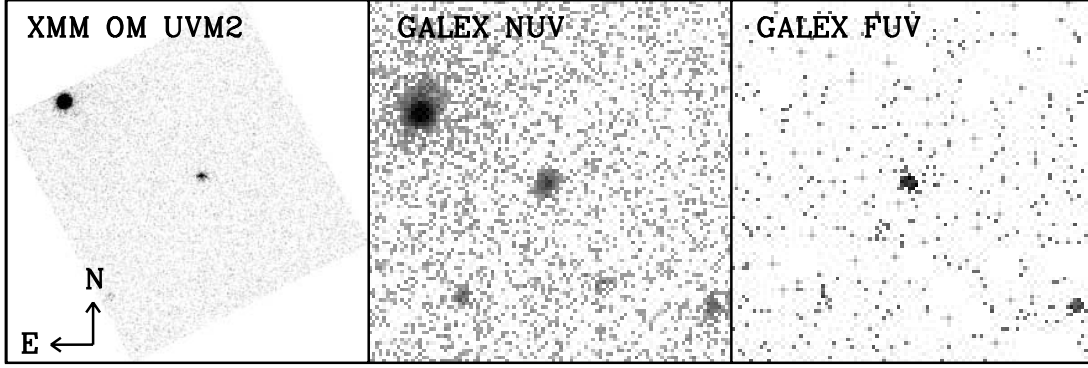
Fɪɢ. 10.—Ultraviolet images of POX 52 (*central object in each panel*). Each image is 150″ on a side. The OM panel is a single 1 ks image taken from our sample of 72 images.

column density is 3 times that needed to model the *Chandra* data, and the model adds a partial covering absorbing column density of $58^{+8.4}_{-9.2} \times 10^{21}$ cm^{-2} with a partial covering fraction of $94^{+2.2}_{-3.3}$ %. Since the partial covering fraction is very high, we tested forcing the fraction to 100% or simply using one larger absorbing column density, but both scenarios tended to over-absorb the power law in the soft X-ray end. The unabsorbed luminosity calculated for the *XMM-Newton* observation is within the 1 σ uncertainty of the *Chandra* unabsorbed luminosity, which suggests that the properties of the central engine itself did not change significantly between these two observations. The factor of 4 flux difference between the two X-ray observations is then explained by the additional absorption needed to fit the *XMM-Newton* spectra.

4. ULTRAVIOLET OBSERVATIONS

4.1. *XMM-Newton Optical Monitor*

The Optical Monitor (OM) on *XMM-Newton* took a series of 72 images simultaneously with the X-ray observation, using the UVM2 filter, which is centered at 2310 Å, extending from ~1900 to 2950 Å (FWHM of the PSF = 1.8″ ~ 4 pixels). Each of these images had an exposure time of 1 ks. The images were processed using the *XMM-Newton* SAS routine `omichain` to output calibrated photometric data via aperture photometry. Out of 72 images, POX 52 was easily detected in 60 images by the source detection algorithm in `omichain` and can be seen as the central object in Figure 10. Five additional images were re-processed with `omprep`, `omdetect`, `ommag`, `ommodmap`, and `ommat` separately in order to detect POX 52 by varying the detection threshold. For the remaining seven images, the `omichain` routine was unable to detect or measure the source count rate due to high background count rates, and these images were discarded.

We used the photometric results of `omichain` to construct a UV light curve, shown in Figure 11. The measured flux was corrected for Galactic extinction by using the Schlegel et al. (1998) reddening maps and averaging the Cardelli et al. (1989) extinction law over the OM passband, resulting in $A_{OM} = 0.32$ mag for the UVM2 filter. The mean flux density over the set of observations is $f_\nu(2310\,\text{Å}) = (1.5 \pm 0.1) \times 10^{-27}$ ergs cm^{-2} s^{-1} Hz^{-1}. Inspection of the light curve shows that the source is not highly variable in the UV. Only 25% of the individual points differ from the mean flux level by more than 1 σ, and only 3/64 (or 5%) of the points differ from the mean flux by more than 2 σ; there are no 3 σ outliers. The observed variability is therefore generally consistent with the expected level of variations from photon-counting statistics for a constant source. To further quantify any possible variability, we calculated the normalized excess vari-

ance of the light curve, following the prescription described by Nandra et al. (1997a):

$$\sigma^2_{\text{nxs}} = \frac{1}{N\mu^2} \sum_{i=1}^{N} \left[(X_i - \mu)^2 - \sigma_i^2 \right], \qquad (1)$$

where X_i denotes the count rate of the ith point in the light curve, σ_i is its uncertainty, μ is the mean of the X_i values over the entire light curve, and N is the number of points in the light curve. The resulting excess variance is very small and actually has a negative value: $\sigma^2_{\text{nxs}} = -0.0029$. This result confirms that there is no evidence for significant variability in the UV light curve. The negative value of σ^2_{nxs} implies that the error bars on the measurements are most likely slightly overestimated by the SAS processing and detection algorithm.

4.2. *GALEX*

As part of the *GALEX* All-sky Imaging Survey (AIS), POX 52 was imaged simultaneously in the near-UV (NUV) and far-UV (FUV) bands on 2006 February 9 UT for a total of 114 s.
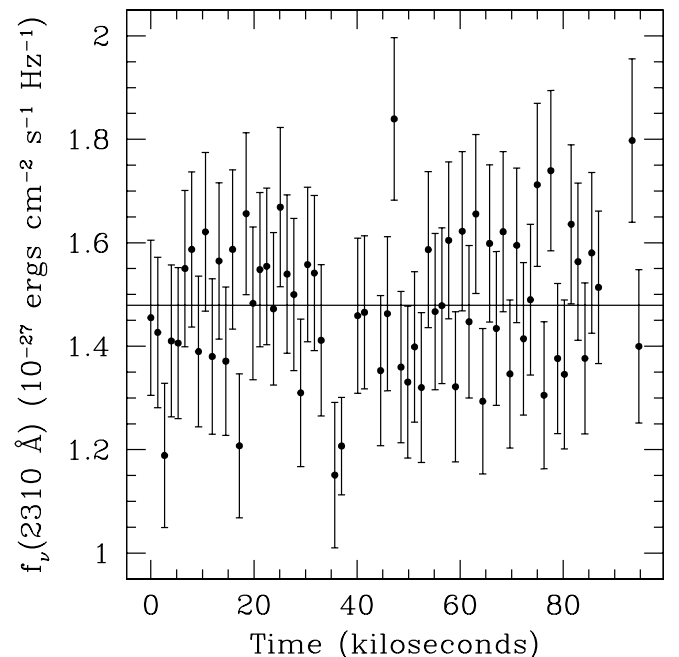

Fɪɢ. 11.—UV light curve of POX 52 from the OM on board *XMM-Newton*. The horizontal line represents the mean observed flux.

The NUV and FUV bands span the ranges 1771–2831 Å and 1344–1786 Å, respectively, with effective wavelengths of 2271 and 1528 Å. The FWHM of the PSF for the NUV filter is 4.0″ ($\sim$2–3 pixels) and for the FUV filter is 5.6″ ($\sim$3–4 pixels). Figure 10 shows both NUV and FUV images of POX 52 alongside one taken with the OM on *XMM-Newton*. Galactic extinction was calculated using the same method as for the OM, resulting in $A_{NUV} = 0.43$ mag and $A_{FUV} = 0.84$ mag. These were then used to correct the fluxes of POX 52 taken from the AIS catalog, resulting in an NUV flux density of $f_\nu(2271 \text{ Å}) = (1.88 \pm 0.08) \times 10^{-27}$ ergs cm^{-2} s^{-1} Hz^{-1} and an FUV flux density of $f_\nu(1528 \text{ Å}) = (1.82 \pm 0.10) \times 10^{-27}$ ergs cm^{-2} s^{-1} Hz^{-1}. The NUV band of *GALEX* surrounds the UVM2 filter on the OM, giving us the opportunity to check for long-term variability in the UV. The flux densities calculated from both instruments are consistent within the 2σ uncertainty range, meaning that we see no significant change in UV luminosity in the 7 months between the separate observations.

In order to estimate the UV host galaxy contribution, we take the observed range of NUV $- V$ and FUV $- V$ colors of Virgo dwarf elliptical galaxies from Boselli et al. (2005) and compute possible NUV and FUV flux densities based on the previous measurement of $V_{host} = 17.4$ mag for POX 52 from Barth et al. (2004). This results in an estimated host galaxy magnitude in the range of NUV = 20.4–22.4 mag (AB) and FUV = 21.9–24.9 mag (AB), which we convert to a host galaxy NUV flux density of $f_\nu(2271 \text{ Å}) = (2.5\text{–}4.0) \times 10^{-29}$ ergs cm^{-2} s^{-1} Hz^{-1} and an FUV flux density of $f_\nu(1528 \text{ Å}) = (4.0\text{–}63) \times 10^{-30}$ ergs cm^{-2} s^{-1} Hz^{-1} for POX 52. We take the average flux density value in each of these bands to correct for host galaxy contamination and find corrected AGN flux densities of $f_\nu(2271 \text{ Å}) = 1.85 \times 10^{-27}$ ergs cm^{-2} s^{-1} Hz^{-1} and $f_\nu(1528 \text{ Å}) = 1.80 \times 10^{-27}$ ergs cm^{-2} s^{-1} Hz^{-1} for the NUV and FUV, respectively. Correcting the OM measurement in a similar manner results in a negligible change to the flux density. We note that, even for the highest estimate of host galaxy UV flux, the source is still very AGN dominated in the UV.

5. RADIO OBSERVATIONS

POX 52 was observed for 1 hr on 2004 October 10 UT with the VLA in A configuration (Thompson et al. 1980), as part of a larger program to observe low-mass active galaxies from Greene & Ho (2004; see Greene et al. 2006). Observations were carried out at 4.860 GHz (6 cm; C band) with a bandwidth of 50 MHz for each of two intermediate frequencies separated by 50 MHz. For purposes of phase calibration, observations of the target were alternated every 3–5 minutes with observations of a bright radio source (PKS J1159$-$2148, located $\sim$1° away). Our overall flux scale is tied to 3C 48, with an assumed flux density of 5.4 Jy, and uncertainties in the absolute fluxes of the phase calibrators, estimated to be $\sim$5%, dominate the flux scale uncertainties.

After removal of corrupted records, flux and phase calibration was performed within AIPS (Greisen 2003). We then Fourier transformed the observed visibilities to create an image of intensity on the sky, using a pixel scale of 0.06″ and a resulting synthesized beam of $\Delta\theta \approx 0.6″$. We find no confusing sources within the primary beam ($\sim$9′), and so, because deconvolution algorithms such as CLEAN may change the noise statistics in a source-free image, we have calculated the upper limit of 0.078 mJy directly from the direct Fourier transform. This upper limit represents 3 times the measured noise limit in the uncleaned map of 0.026 mJy and corresponds to a radio power of $P < 8.1 \times 10^{19}$ W Hz^{-1} and a radio-loudness parameter ($R \equiv f_{6\,cm}/f_{4400\,Å}$)
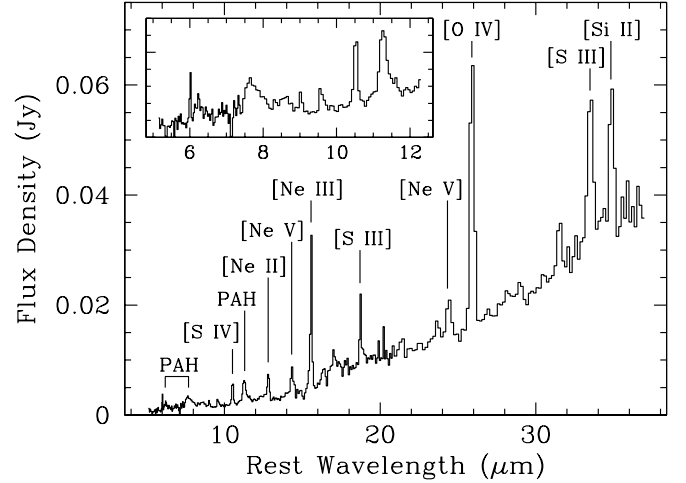

Fig. 12.—*Spitzer* IRS spectrum of POX 52 from 5 to 38 μm. The most prominent spectral lines are identified. The inset shows a close-up of the 5–12 μm region.

for POX 52 of $R < 0.28$, where a radio-loud object is usually defined to have $R \geq 10$ (Kellermann et al. 1989).

These values are consistent with the majority of the other GH sample sources studied by Greene et al. (2006). Out of 19 objects studied, Greene et al. (2006) only significantly detected 1 object, with 3σ upper limits to the radio power of the other 18 objects around $P <$ few $\times 10^{21}$ W Hz^{-1}. The high upper limits for the GH objects relative to POX 52 are due to the larger distances to the GH sample. The upper limits on the radio-loudness parameter may be a better comparison between POX 52 and the GH objects, which range from $R < 0.68$ to $R < 9.9$ for the GH sample, but the majority of these objects are well below the $R \geq 10$ cutoff that usually describes a radio-loud object. Stacking the GH sample results in $R < 0.27$, giving a stricter upper limit to the radio loudness of the sample as a whole.

6. INFRARED OBSERVATIONS

6.1. *Spitzer Space Telescope*

POX 52 was observed on 2006 July 24 UT with the *Spitzer* IRS (Houck et al. 2004) as part of a sample of low-mass Seyfert galaxies (program ID: 30119). The analysis of the entire sample, including measurements of emission lines and continuum shape, will be presented in a later paper, but we include the POX 52 spectrum here in order to supplement our multiwavelength coverage of this object. It was observed in the Short-Low and Long-Low slit modes, which correspond to a total wavelength range of 5.2–38 μm. Exposure times were 2×60 s each in the SL1 and SL2 settings and 2×120 s each in the LL1 and LL2 settings. Data were processed prior to download with IRS Pipeline Processing version 15.3.0. Data were first cleaned using the IDL routine IRSCLEAN (ver. 1.9), and the images were then co-added following the procedure in the Infrared Spectrograph Data Handbook[11] (ver. 3.1). The spectrum from each slit was extracted and calibrated using SPICE (ver. 2.1.2). For each slit, the two nod positions were subtracted from each other in order to sky subtract the resulting data. Spectra from each of the four slits were combined and any overlapping data from adjacent wave bands were averaged together in the final product. Data from the LL slit were multiplied by a factor of 1.4 in order to properly match data from the SL slit. Figure 12 shows the combined spectrum with the most

---

[11] See http://ssc.spitzer.caltech.edu/irs/dh/.

prominent emission lines identified, including [Ne II] 12.81 μm, [Ne III] 15.56 μm, [Ne V] 14.32 μm, [O IV] 25.89 μm, [S III] 18.71 and 33.48 μm, [S IV] 10.51 μm, [Si II] 34.82 μm, and polycyclic aromatic hydrocarbon (PAH) features at 6.2, 7.7, and 11.3 μm.

The IRS spectra of POX 52 show possible weak silicate absorption near 10 μm seen in some Seyfert 1 galaxies, but more commonly associated with Seyfert 2 galaxies (Hao et al. 2007). Assuming a power-law fit over the 30–20 μm range with $f_\nu \propto \nu^{-\alpha}$, POX 52 shows a steeper spectral slope $\alpha_{30-20} \approx 2.1$ than many Seyfert 1 galaxies (Buchanan et al. 2006). The spectral slope from 15 to 6 μm of $\alpha_{15-6} \approx 1.16$ is significantly flatter than α_{30-20}, suggesting the best continuum fit to be a broken power law, which is often seen in Seyfert 1 spectra (Weedman et al. 2005). The presence of PAH features and the observed red continuum (seen as the steep α_{30-20} slope) suggests possible star formation in the host galaxy; however, we defer any further analysis to the later paper on the full *Spitzer* sample.

6.2. *2MASS Point Source Catalog*

Near-infrared magnitudes were taken from the 2MASS Point Source Catalog (Skrutskie et al. 2006) in the J (15.7 mag), H (15.0 mag), and K_s (14.5 mag) bands to be included along with our other data in the SED (see Fig. 15 below). These magnitudes include flux from the host galaxy as well as the AGN. In order to correct for this, we used averaged $B - J = 2.05$, $B - H = 2.57$, and $B - K = 2.67$ color indices derived from photometry of 10 dwarf ellipticals in the Virgo Cluster (James 1994). Our GALFIT estimate of the B-band $m_{\rm host}$ (corrected from the F435W ACS HRC filter to the standard Johnson B filter using the IRAF routine `calcphot`) was used in order to estimate the JHK contribution from the host galaxy. The host galaxy contributions were then subtracted from the 2MASS magnitudes, resulting in the following AGN point-source JHK magnitude estimates: $J_{\rm AGN} = 16.8^{+0.8}_{-0.6}$ mag, $H_{\rm AGN} = 15.8^{+0.8}_{-0.5}$ mag, and $K_{\rm AGN} = 15.0^{+0.6}_{-0.8}$ mag. The errors were calculated based on the range of $B - J$, $B - H$, and $B - K$ colors for dwarf elliptical galaxies derived from James (1994).

7. DISCUSSION

7.1. *Host Galaxy Structure*

Barth et al. (2004) previously classified POX 52 as a dwarf elliptical based on its morphology, their measurements of $M_B = -16.8$, $r_e = 1.2''$, and $n = 3.9$, and the location of POX 52 in the "κ-space" projections (Bender et al. 1992; Burstein et al. 1997) of the fundamental plane. These κ parameters combine stellar velocity dispersion, surface brightness, and effective radius together in such a way, which correspond to the physical parameters of stellar mass and mass-to-light ratio, that a clear split can be seen among giant ellipticals, dwarf ellipticals, dwarf spheroidals, and globular clusters. In these projections, POX 52 falls nearest the Virgo dwarf elliptical galaxies from Geha et al. (2003) and is offset only slightly toward a higher surface brightness and a lower mass-to-light ratio. Our new *HST* observations do little to change the location of POX 52 in these projections, as the surface brightness and effective radius found in this paper are consistent with the previous values.

The addition of similar objects from the GH sample, based on new *HST* imaging (Greene et al. 2008), to these fundamental plane relations suggests that they are more centrally concentrated than typical dwarf ellipticals. However, in plots of μ_e versus M_V and r_e versus M_V, they reside in between the distributions of dwarf ellipticals and classical ellipticals, as a possibly intermediate population. These galaxies clearly have properties that are in

common with both populations, but they follow the distribution of dwarf ellipticals when kinematic data are combined with photometric data in the "κ-space" projections; therefore, we conclude that POX 52 and similar objects are most closely related to dwarf ellipticals, although they remain unusual for having unexpectedly highly Sérsic indices.

We note a difference in terminology between what some authors call a dwarf elliptical galaxy (Binggeli & Jerjen 1998; Geha et al. 2002) and a different designation, spheroidals, in order to distinguish the typically less centrally concentrated objects from low-luminosity versions of classical ellipticals (Kormendy 1985). In this paper we refer to these galaxies as dwarf ellipticals for consistency with the nomenclature adopted in our earlier paper (Barth et al. 2004).

From our GALFIT decompositions, we can conclude that the host galaxy is well fitted in both of the observed filters by a Sérsic profile with $n \approx 4$ and $r_e \approx 1''$ at $r > 0.5''$. The structure of the inner region of the host galaxy remains complicated due to the second Sérsic component needed to provide a reasonable fit in the F435W filter. We noted earlier that the inner Sérsic component seems to be compensating mostly for the PSF mismatch, but its broader profile suggests the possibility of a spatially compact, blue component, such as a nuclear star cluster. Looking at the $B - I$ color of POX 52 with and without the inner Sérsic component included, we can bracket the range of possible colors of the host galaxy. Excluding the inner Sérsic component, we find $B - I = 2.0$ for the host galaxy, which is similar to fiducial values ($B - I = 2.0$–2.1) for S0/Sab galaxies found in Fukugita et al. (1995) and from SYNPHOT calculations ($B - I = 2.2$–2.3) with the Kinney et al. (1996) S0/Sab galaxy templates. If we assume that the compact component is entirely due to starlight, the resulting color of $B - I = 0.74$ is bluer than both the Fukugita et al. (1995) fiducial value for Im galaxies ($B - I = 0.9$) and all of the starburst galaxy templates ($B - I = 0.9$–1.6) from Kinney et al. (1996). Therefore, we conclude that the inner Sérsic component in the F435W image must contain a substantial amount of light from the AGN point source. However, we cannot determine the exact fractions of AGN light and starlight in this component. This leaves a wide range of possible colors for the host galaxy.

7.2. *X-Ray Spectral Properties*

X-ray spectral variability is not an unusual occurrence in an AGN but is normally manifested in small changes in the spectral slope or in the width or amplitude of an emission line. Strong variability in the absorbing column density is more rare but is often attributed to partial covering. In this scenario, there exists a patchy absorber surrounding the AGN made up of many smaller gas clouds orbiting the central engine with close to Keplerian velocities. The variations seen in column density are therefore related to the number of clouds along the line of sight. This has become a common model to use when a change in the spectral slope on the soft end is observed, as has been seen in several NLS1 galaxies, including IRAS 13224−3809 (Boller et al. 2003; Gallo et al. 2004a), RX J2217.9−5941 (Grupe et al. 2004a), Mrk 335 (Grupe et al. 2007), Mrk 1239 (Grupe et al. 2004b), and 1H 0707−495 (Gallo et al. 2004b).

The bright NLS1 Mrk 335 has recently experienced a change in absorption very similar to what we observe in POX 52. Mrk 335 has regularly been studied in the X-rays since 1971 with no dramatic changes in flux until 2007, when Grupe et al. (2007) measured a factor of 30 decrease in flux compared to all previous observations. When the spectra were modeled, Grupe et al. (2007) were unable to obtain a good fit with scaled-down versions of

previously used models and found that adding a partial covering model to an absorbed power law with a high partial covering fraction of 0.9–1, much like that of POX 52, enabled an acceptable fit. When corrected for this additional absorption, the change in intrinsic luminosity is only a factor of 4–6 when compared to earlier observations. Grupe et al. (2007) note that a partial covering model can also reasonably fit their 2006 data with a lower partial covering fraction of $\sim$0.5 but does not result in the best fit for their 2000 data. This suggests that the partial covering absorber was moving into the line of sight as early as 2006.

Assuming that the sizes of these discrete absorbing clouds do not vary much from one source to another and that the accretion disks and surrounding X-ray-emitting regions of less massive black holes like POX 52 are, in fact, scaled-down versions of those associated with their more massive counterparts, one would expect the X-ray absorbing region to be less voluminous and therefore contain fewer absorbing clouds. Furthermore, if the differences in column density are attributed to the number of clouds instead of the size of clouds, it is possible that an X-ray-emitting region surrounding a black hole the size of POX 52 would have a higher likelihood of being observed with almost no absorbing clouds in the line of sight than for a more massive source due to the differences in the number of clouds associated with each source. The black hole in POX 52 is $\sim$2 orders of magnitude less massive than that in Mrk 335 (Peterson et al. 1998, 2004; Vestergaard & Peterson 2006) and moved from an unabsorbed state to the partial covering state in less than 9 months, whereas the change in absorbing column in Mrk 335 occurred over $\sim$1–7 yr (Grupe et al. 2007). These observations give upper limits to the timescales of absorption variability based on the partial covering scenario.

Barth et al. (2004) examined the *Röntgensatellit* (*ROSAT*) all-sky survey image of the position of POX 52 with an exposure time of $\sim$90 s. Although there was no prominent source at the position of POX 52, Barth et al. (2004) showed that there were two counts above the background rate within a circular aperture of radius equal to roughly FWHM of the PSF of the detector, for a 3.0–3.5 σ detection. With this in mind, we used the WebPIMMS[12] online calculator to determine what state POX 52 might have been in when this observation was taken. Inputting our best-fit models from *XMM-Newton* and *Chandra*, we find that the unabsorbed state would have resulted in a 0.4–2.4 keV *ROSAT* detection in the range of 4–14 counts, and the absorbed state would have produced 1–4 counts during the observation. From this we conclude that the *ROSAT* flux is consistent with the *XMM-Newton* absorbed state, or possibly a lower luminosity state. Further observations would help determine the more common X-ray state of POX 52 and better constrain the timescales of this variability.

We see no change in the intrinsic power-law spectral slope of $\Gamma \approx 1.9$ between these two observations. This is somewhat unusual given the large amount of both short-term ($\sim$500 s) and long-term ($\sim$$10^7$ s) variability that characterizes many NLS1 galaxies, including POX 52. For example, POX 52's most similar companion, NGC 4395, has been shown to have strong variations not only in flux (factor of 2 over 5 months; O'Neill et al. 2006) but also in spectral slope ($\Gamma \approx 0.6$–1.7 over 2 yr; Moran et al. 2005). A 2–10 keV spectral slope of 0.6 is unusually low for either a Seyfert 1 galaxy or an NLS1 galaxy; a slope of $\sim$2 is far more common for Seyfert 1 galaxies, NLS1 galaxies, and quasars (Crummy et al. 2006; Leighly 1999b; Piconcelli et al. 2005). The temperature of the blackbody component, used to model the soft excess seen in many NLS1 galaxies, also remained unchanged

for POX 52 between the two observations, with a temperature of $kT = 0.13$ keV that is within the normal range (0.1–0.3 keV) seen in NLS1 galaxies (Leighly 1999b). When NLS1 spectra with soft excesses are fitted with a model consisting of only a power-law or absorbed power-law component, the result is a steep spectral slope of $\Gamma \approx 3$–5 (Boller et al. 1996), as opposed to the more common NLS1 spectral slope of $\Gamma \approx 2$.

In comparison, the similar low-mass GH sample objects observed with *Chandra* also have slightly different X-ray properties (Greene & Ho 2007a). These 10 objects were observed for 5 ks each, resulting in only five objects with enough counts to allow for spectral fitting, and even this could only be done in the 0.3–5 keV range. A soft photon index was derived from the hardness ratios for each object, giving a range of $1 < \Gamma_S < 2.7$ for the sample that brackets the 0.5–10.0 keV photon index for POX 52. The GH sample objects show no signs of either a soft excess or intrinsic absorption. The observations did not allow for study of short-term variability due to low count rates.

Miniutti et al. (2008) reobserved four of these GH objects with *XMM-Newton* for 20–30 ks, in order to obtain a high enough signal-to-noise ratio for spectral fitting. These objects have remarkably similar spectra in the 0.5–10.0 keV range to the *Chandra* spectrum of POX 52, and fits with power-law plus disk blackbody models produce photon indices in the range of $1.8 < \Gamma < 2.5$ and temperatures of $\sim$0.11 keV. Although the blackbody temperature of the soft excess is similar to what is seen in both the *Chandra* and *XMM-Newton* observations of POX 52, the hard photon index of these GH objects is, on average, slightly harder than what has been observed in POX 52. These objects are an order of magnitude more luminous in the X-ray than POX 52, and they contain black holes with masses around an order of magnitude larger than POX 52 (Greene & Ho 2007b).

7.2.1. *Power Spectral Density*

AGNs are highly variable in X-rays, and with good data sampling, one can study the frequency dependence of these variations by computing the power spectrum density (PSD), which is a measure of the amount of variability at a given frequency. The PSDs of AGNs and Seyferts are often fitted with a combination of two power laws with a slope of -2 at the high-frequency end and then breaking to a slope of -1 at the low-frequency end. The frequency at which this change occurs is known as the break frequency, ν_B, and appears to correlate inversely with black hole mass (Markowitz et al. 2003).

Since the *Chandra* data have a higher signal-to-noise ratio than the *XMM-Newton* data and more closely represent the intrinsic state of the central engine without the heavy obscuration seen with *XMM-Newton*, we chose to carry out the PSD analysis on the *Chandra* data set. We start by creating a light curve using 100 s time bins covering the 0.5–10.0 keV energy range. The XRONOS (ver. 5.21) tool `powspec` (ver. 1.0) was used to create the PSD from the light curve and can be seen in Figure 13 binned by a factor of 5 in frequency in order to increase the signal-to-noise ratio. There may be a possible flattening of the PSD from low frequencies and a break to a steeper slope at $\sim$$3 \times 10^{-4}$ Hz. However, the PSD is easily fitted with a single power law with a best-fit slope of -0.94 and a $\chi^2 = 2.87$ for 8 dof. This fit is good enough that a broken power-law fit is not justified. To test whether any constraints on ν_B could be derived, we attempted to fit a broken power law to the data. Unfortunately, all attempts at fitting the data while allowing parameters to vary freely produced either a break frequency outside the range of our data or a broken power law with no break, and the result is that both power-law models had identical slopes. Arbitrarily forcing a specific break frequency
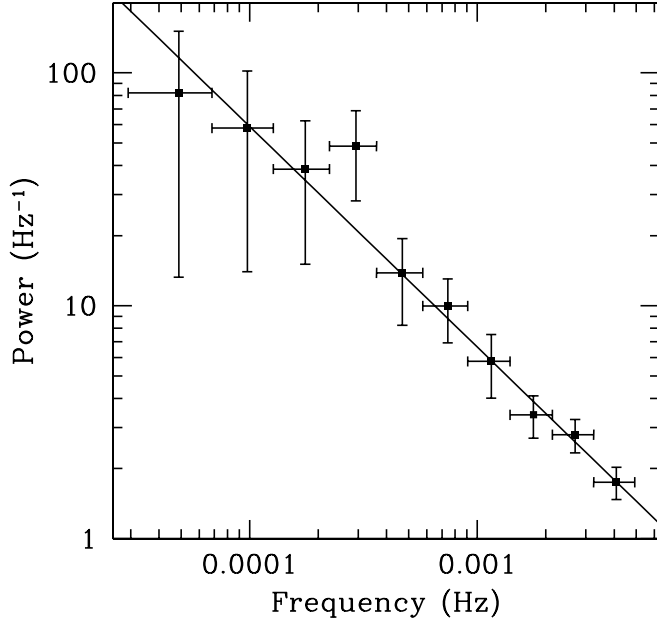
Fig. 13.—PSD derived from *Chandra* data using a light curve with 100 s time bins. The PSD itself has been binned by a factor of 5. A power law with slope −0.95 is shown as a solid line.

Fig. 14.—Plot of σ_{nxs}^2 vs. 2–10 keV luminosity. NLS1 data from Leighly (1999a, 1999b) are shown as filled circles. Classical Seyfert 1 data from Nandra et al. (1997a, 1997b) are shown as open circles. POX 52 is shown as a red (*Chandra* data) or a blue (*XMM-Newton* data) cross. The unabsorbed luminosity is used for the *XMM-Newton* data point in order to represent the intrinsic luminosity of the source. Similar low-mass objects from the GH sample are shown as open triangles (Miniutti et al. 2008), including NGC 4395 (Iwasawa et al. 2000) as a filled triangle.

produced fits to the data with low-frequency slopes of roughly −0.3 and high-frequency slopes of roughly −1.4, neither of which approximate the expected slopes of −1 and −2 seen in most AGNs and Seyferts. From this we conclude that if ν_B is actually within the range detectable from our data, our PSD is of such low quality that we are unable to measure it, or alternatively, ν_B lies at a frequency higher than $\sim 5 \times 10^{-3}$ Hz.

Even without an accurate measurement of ν_B, we can still gain information from the relationship between excess variance and L_X. There seems to be a noticeable split between the distribution of σ_{nxs}^2 for NLS1 and classical Seyfert 1 galaxies, with the excess variance of the NLS1 galaxies consistently larger than that of the Seyfert 1 galaxies at a given luminosity (Leighly 1999a). To test this for the low-mass case of POX 52, we calculate the excess variance from the entirety of the usable light curve for both our *XMM-Newton* (second half of the observation, $\sim$50 ks) and *Chandra* ($\sim$25 ks) data, using 500 and 100 s bins, respectively, and plot the results against the 2–10 keV unabsorbed luminosity, along with NLS1 data from Leighly (1999a, 1999b), Seyfert 1 data from Nandra et al. (1997a, 1997b), and GH object data from Miniutti et al. (2008), in Figure 14. From this analysis, we find the excess variance of the two observations to be quite similar, $\sigma_{\mathrm{nxs}}^2(Chandra) = 0.0388 \pm 0.0003$ and $\sigma_{\mathrm{nxs}}^2(XMM\text{-}Newton) = 0.0494 \pm 0.0073$, despite the substantial additional absorber present in the *XMM-Newton* observation. This suggests that in the case of POX 52, the variability seen in the *XMM-Newton* observation is due to intrinsic variability and not due to fluctuations in the partial covering or the absorbing column density.

7.3. *Spectral Energy Distribution*

We combine all of our data and present one of the most complete SEDs (Fig. 15, Table 4) of a low-mass AGN to date, covering the radio to the X-ray. For comparison, we include the templates of Elvis et al. (1994) from Palomar-Green (PG) quasars (Schmidt & Green 1983), normalized to the flux of our NUV *GALEX* data point. The data from our observations closely match those of the radio-quiet (RQ) template for the majority of the frequency range shown. The *Chandra* data show POX 52 as
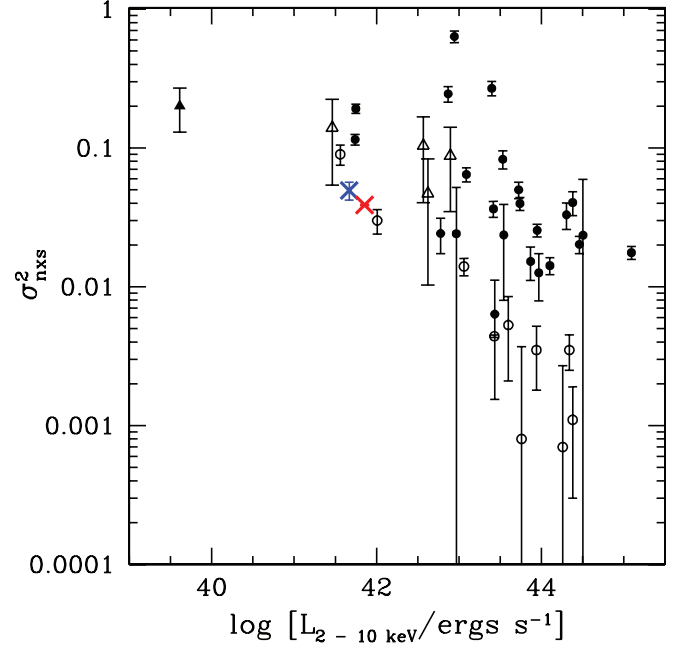
X-ray bright compared to the RQ template, and we again note that the *XMM-Newton* data represent a period of high absorption, not a decrease or change in the flux of the central object itself. It should also be noted that the observations are nonsimultaneous and could therefore represent POX 52 in various states of emission, so care should be taken in examining the SED and comparing fluxes from different observations.

We approximate the shape of the SED near the OM observations as a power law with $f_\nu \propto \nu^{-1}$ and extract a UV luminosity at 2500 Å of 1.5×10^{27} ergs s^{-1} Hz^{-1}. Combining this with the 2 keV unabsorbed luminosity derived from the simultaneous observations with the EPIC cameras on *XMM-Newton*, we can calculate α_{ox}, the slope of a hypothetical power law connecting the UV to the X-ray[13] (Tananbaum et al. 1979). We find $\alpha_{\mathrm{ox}} = -1.3$, and this value does not change on substitution of the *Chandra* 2 keV unabsorbed luminosity. Strateva et al. (2005) studied α_{ox} in a sample of 228 optically selected AGNs and found that α_{ox} decreased with increasing luminosity. This correlation has been updated by Steffen et al. (2006) to include higher redshift objects, resulting in $\alpha_{\mathrm{ox}} = -0.137 L_{\mathrm{UV}} + 2.638$, where L_{UV} is the luminosity of the object measured at 2500 Å. We plot the data from Strateva et al. (2005) along with those of POX 52 and similar intermediate-mass black holes from Greene & Ho (2007a) in Figure 16, showing that POX 52 falls among its intermediate-mass counterparts and within the 1 σ errors of the extrapolated correlation between α_{ox} and UV luminosity calibrated for more luminous type 1 AGNs from Steffen et al. (2006).

Using the Elvis et al. (1994) UV bolometric correction, we estimate $L_{\mathrm{bol}} \approx 1.1 \times 10^{43}$ ergs s^{-1} from the OM observations. Repeating this with the Elvis et al. (1994) *B*-band correction

---

[13] If a power law of the form $f_\nu \propto \nu^{\alpha_{\mathrm{ox}}}$ is assumed, α_{ox} is then defined by $\alpha_{\mathrm{ox}} = 0.3838 \log [f_\nu(2\ \mathrm{keV})/f_\nu(2500\ \text{Å})]$.
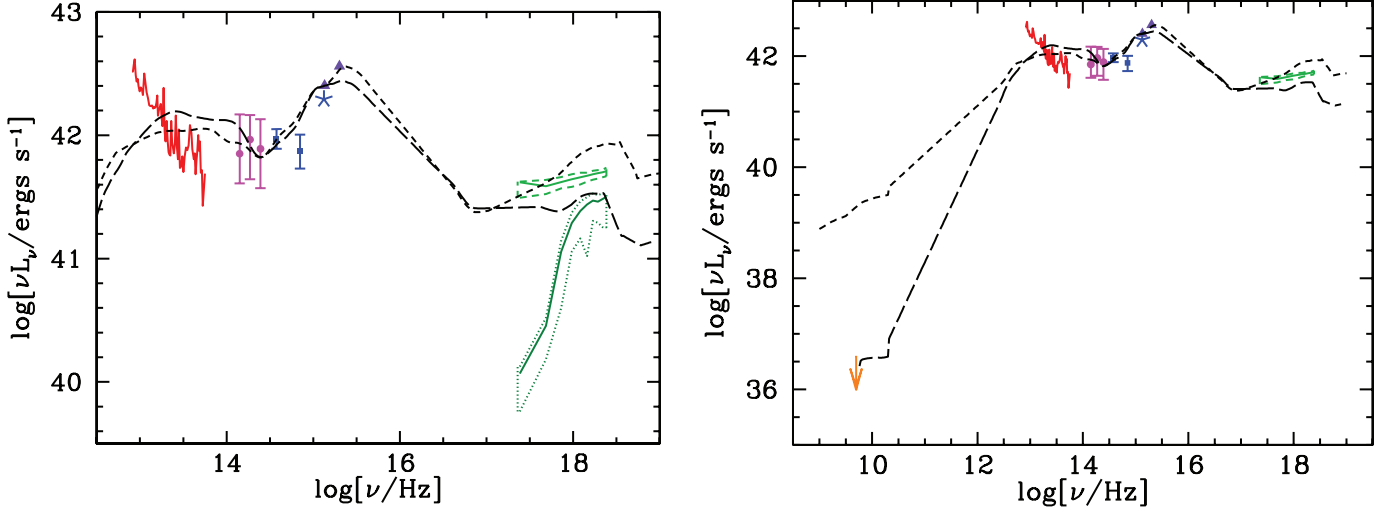
Fig. 15.—SED of POX 52. The dashed lines are the radio-loud (*short-dashed line*) and radio-quiet (*long-dashed line*) SED templates from Elvis et al. (1994) normalized to the UV data point. The X-ray data are in green with the dotted (*Chandra*) and dashed (*XMM-Newton*) lines representing the 1 σ uncertainty range for the respective observatories. The *HST* (*squares*) and OM (*asterisk*) data are in blue, the magenta circles are from 2MASS, the purple triangles are from *GALEX*, the red spectrum is from *Spitzer* IRS (binned by a factor of 5 for clarity), and the gold arrow represents the upper limit on the VLA data. The left panel shows a close-up of the IR to X-ray data, and the right panel shows the full extent of the data, excluding the strongly absorbed *XMM-Newton* observation.

and the *HST* measurement results in $L_{bol} \approx 6.5 \times 10^{42}$ ergs s^{-1}, which is a factor of ~2 smaller than that of the UV data. Both of these estimates are based on observations of POX 52 in a single band, constituting a single point each on the SED. Using the templates derived by Elvis et al. (1994) shown on the SED, we estimate the L_{bol} using all of the data collected. With the templates normalized to match the *GALEX* NUV luminosity of POX 52, the radio-quiet template matches most data points at frequencies less than 10^{16} Hz, including the upper limit in the radio. We integrate the radio-quiet template from 6 cm to 1 keV and the *Chandra* data from 1 to 10 keV and estimate the bolometric luminosity based on the full extent of our data to be L_{bol}(SED) $\approx$ 1.3×10^{43} ergs s^{-1}, which is consistent with the value estimated from the UV correction. We take this value as our best estimate of L_{bol}.

7.4. Black Hole Mass

For Seyfert 1 galaxies and quasars, there exists a correlation between the radius of the broad-line region (r_{BLR}) and the lumi-

nosity of the optical nonstellar continuum (most often measured at 5100 Å), $r_{BLR} \propto L^{\beta}$. Kaspi et al. (2000) derived this relationship based on their observations of 17 reverberation-mapped PG quasars combined with the results of 17 lower luminosity AGNs with reverberation data. This relationship was recently updated by Bentz et al. (2006) by taking into account the host galaxy starlight contamination. Using this relation in tandem with the virial relation, $M_{BH} = fr_{BLR}\Delta V^2/G$, one can estimate the mass of a black hole with a single spectrum. However, the normalization and slope in the radius-luminosity relation and the value of the normalization factor f in the virial relation, which depends on the geometry and kinematics of the broad-line region,
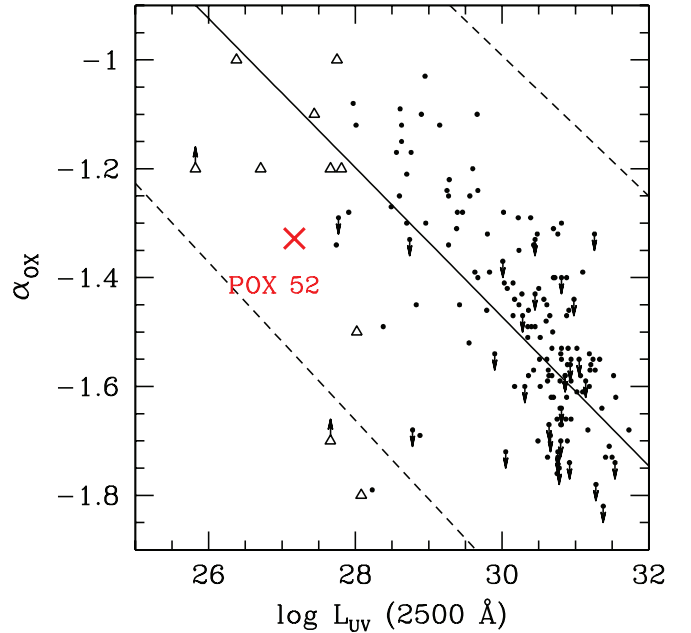
TABLE 4
SED DATA

Rest Wavelength or Energy	log (νL_ν/ergs s^{-1})	Source
6 cm	<36.127	VLA
36 μm...	42.58	*Spitzer* IRS
30 μm...	42.39	*Spitzer* IRS
20 μm...	42.22	*Spitzer* IRS
10 μm...	41.75	*Spitzer* IRS
6 μm...	41.70	*Spitzer* IRS
2.12 μm...	41.85	2MASS K_s
1.61 μm...	41.97	2MASS H
1.22 μm...	41.89	2MASS J
7966 Å	41.97	*HST* F814W
4257 Å	41.88	*HST* F435W
2260 Å	42.29	*XMM-Newton* OM
2222 Å	42.40	*GALEX* NUV
1495 Å	42.56	*GALEX* FUV
1.0 keV...................................	41.62	*Chandra*
2.0 keV...................................	41.59	*Chandra*
10.0 keV...................................	41.71	*Chandra*

Fig. 16.—Plot of α_{ox} vs. UV luminosity. Black dots are luminous type 1 AGNs from Strateva et al. (2005), arrows represent upper limits, the open triangles are intermediate-mass black holes from Greene & Ho (2007a), and the red cross is POX 52 derived from simultaneous UV and X-ray data taken with *XMM-Newton*. The solid line is the linear relation from Steffen et al. (2006), and the dashed lines represent the 1 σ error on that relation.

are still subject to considerable uncertainty. In addition, different permutations of this relation not only use different emission lines for the line width measurement ΔV, but they also measure ΔV in different ways, either using the FWHM or the line dispersion (σ_{line}). Onken et al. (2004) calibrated the average normalization factor, $f = 1.4$, by assuming that all AGNs follow the same M_{BH}-σ_* relation as quiescent galaxies.

We rely on the previous measurement of the Hβ line width from a high-resolution Keck spectrum by Barth et al. (2004). They fitted the broad Hβ line with a Gaussian model and found $v_{FWHM} = 765$ km s^{-1}. The conversion from FWHM to σ_{line} for a Gaussian fit is $\sigma_{line} =$ FWHM/2.35.

Using the radius-luminosity relation of Kaspi et al. (2000) and the broad Hβ line width of $v_{FWHM} = 765$ km s^{-1} discussed above, Barth et al. (2004) previously estimated the black hole mass of POX 52 to be $M_{BH} \approx 1.6 \times 10^5$ $M_\odot$. We start our new calculation of black hole mass using the combined revisions of Bentz et al. (2006) and Onken et al. (2004), as well as our new *HST* measurements, such that

$$ M_{BH} = 1.05 \times 10^7 \left[\frac{\lambda L_\lambda (5100\ )}{10^{44}\ \text{ergs s}^{-1}} \right]^{0.518} \left(\frac{v_{FWHM}}{10^3\ \text{km s}^{-1}} \right)^2 M_\odot. $$

(2)

We note that our *HST* imaging is nonsimultaneous with the previous Keck spectrum from Barth et al. (2004) and therefore potentially introduces some error in the M_{BH} calculation due to source variability. The extinction-corrected point-source absolute magnitude calculated from the GALFIT decomposition is $M_{F435W}(\text{PSF}) = -15.7$. For comparison, we also calculate the extinction-corrected absolute magnitude needed to maximize the PSF contribution to the galaxy, $M_{F435W}(\text{PSF}_{max}) = -16.3$. These two magnitudes correspond to a range of $\lambda L_\lambda(5100\ \text{Å}) = (3.2-5.6) \times 10^{41}$ ergs s^{-1}. Using $v_{FWHM} = 765$ km s^{-1} from Barth et al. (2004), we calculate $r_{BLR} = 2.0-2.7$ lt-day and $M_{BH} \approx (3.1-4.2) \times 10^5$ $M_\odot$.

As noted earlier, there are many different recipes to estimate black hole mass that rely on different versions of the radius-luminosity and virial mass relations. McGill et al. (2008) recently compiled a list of some of the most common versions, and we use their formulations to explore the range of possible M_{BH} values in POX 52. We eliminate those relations in which the slope of the radius-luminosity relation is ≥ 5.5, which contradicts the updated measurement of Bentz et al. (2006), and are left with three alternate relations (eqs. [8], [10], and [13] of McGill et al. 2008). We use the same parameters above from our *HST* measurements and the v_{FWHM} from Barth et al. (2004) and find a range of black hole masses of $M_{BH} \approx (1.8-2.7) \times 10^5$ $M_\odot$ for POX 52, with an average of $\langle M_{BH} \rangle = 2.2 \times 10^5$ $M_\odot$. This then extends our total range of possible black hole mass to $(1.8-4.2) \times 10^5$ $M_\odot$, increasing the evidence that POX 52 contains an intermediate-mass black hole. This mass range is due to the scatter in using slightly different relations in the calculation of M_{BH}, but the systematic scatter in using any single relation is ~ 0.5 dex (Onken et al. 2004; Vestergaard & Peterson 2006).

7.4.1. *Black Hole Mass Estimates from X-Ray Variability*

Both ν_B and excess variance have been shown to be roughly correlated with black hole mass (Papadakis 2004). We investigate both of these methods in order to independently confirm our mass estimates from optical data. We first estimate the expected ν_B from the properties of the AGN. Markowitz et al. (2003) fitted a simple relation with $1/\nu_B$ measured in days, $1/\nu_B = M_{BH}/10^{6.5}$ $M_\odot$, in

which ν_B is solely dependent on black hole mass. This relation seems to hold quite well for normal Seyfert 1 galaxies, but it underestimates black hole masses calculated from ν_B for NLS1 galaxies, which have been known to have shorter break timescales (and therefore higher break frequencies) than classical Seyfert 1 galaxies with similar black hole masses (Papadakis 2004). In order to try to account for this disparity, McHardy et al. (2006) incorporated bolometric luminosity in the ν_B-M_{BH} relation, in an effort to account for the higher accretion rates seen in NLS1 galaxies compared to the average Seyfert 1. Taking the inverse of $\nu_B = 1/T_B$, where T_B is known as the break timescale, McHardy et al. (2006) found the best fit in the T_B-M_{BH}-L_{bol} plane for their sample of Seyfert 1, NLS1, and Galactic black holes to be $\log T_B = 2.10 \log M_{BH} - 0.98 \log L_{bol} - 2.32$, where T_B is measured in days, M_{BH} is measured in units of 10^6 $M_\odot$, and L_{bol} is measured in units of 10^{44} ergs s^{-1}. We use our average estimate of black hole mass and bolometric luminosity to calculate the corresponding ν_B from each of these relations and find $\nu_B \approx 1.2 \times 10^{-4}$ Hz using the Markowitz et al. (2003) prescription and $\nu_B \approx 3.8 \times 10^{-3}$ Hz using the McHardy et al. (2006) prescription. Since our PSD analysis was unable to determine ν_B, we note that ν_B estimated from the Markowitz et al. (2003) relation occurs near the visual break seen in Figure 13, and ν_B estimated from the McHardy et al. (2006) relation occurs at the high-frequency end of this same plot.

Other recent work has explored alternative methods to correlate the variability in observations too short for PSD analysis with black hole mass. Nikołajuk et al. (2004, 2006) calibrated the relationship between the excess variance of the variability in a given observation and the mass of the black hole. The excess variance must be sampled from the high-frequency end of the PSD, above ν_B where the shape of the PSD is described by $P(\nu) \propto \nu^{-2}$. The cornerstone of this method is the assumption that the amplitude of the PSD at ν_B multiplied by ν_B is constant for all objects and independent of black hole mass, i.e., $P(\nu_B)\nu_B = $ constant. This has been shown to be roughly accurate for a handful of objects studied to date (Markowitz et al. 2003; McHardy et al. 2004; Papadakis 2004). Since the excess variance is simply the integral of the PSD, it can then be related to ν_B and consequently M_{BH}. This technique has only been tested on a few low-mass black holes in other AGNs, namely, NGC 4395 and the NLS1 NGC 4051.

Without a measurement of ν_B for POX 52, we cannot determine that we are sampling the appropriate section of the PSD; therefore, we continue on with the caveat that the mass estimates calculated using this method are tenuous at best. The *Chandra* observation had a higher signal-to-noise ratio than *XMM-Newton* and therefore had a better chance at producing a reasonable result. We are unable to probe timescales shorter than the break timescale predicted by the McHardy et al. (2006) relation, $T_B \approx 279$ s, so we continue with this method using the simpler Markowitz et al. (2003) relation, which gives a wide range of break timescales ($T_B \approx 5460-13,660$ s) corresponding to our full M_{BH} range. We tested the method using time bins of 100 and 500 s and noted no significant difference between the two, except for the fact that using a smaller time bin allows us to divide the observation into a larger number of segments and therefore probe lower break timescales. We calculated black hole masses using segment lengths of $T \approx 2775-12,500$ s with 100 s time bins and segments of length $T_B \approx 6250-12,500$ s with 500 s time bins, resulting in an average black hole mass of $M_{BH} = (3.9 \pm 1.7) \times 10^5$ $M_\odot$, where the errors represent the range of M_{BH} calculated for various T_B. If the break frequency of POX 52 is $\nu_B \approx 10^{-4}$ Hz or lower, then we are able to probe the region above this frequency

and calculate a black hole mass of $M_{BH} \approx 3.9 \times 10^5 \, M_{\odot}$. But if the break frequency is higher, near the $\nu_B \approx 10^{-4}$ Hz predicted by the McHardy et al. (2006) relation, we are unable to explore the region of interest in frequency space and our black hole mass calculations are inconclusive.

7.5. Accretion Luminosity

Using the range of black hole masses we have estimated here, the Eddington luminosity of POX 52 is in the range $L_{Edd} = (2.9–5.5) \times 10^{43}$ ergs s^{-1}. Taking the bolometric luminosity calculated from the SED, we find an estimate of the Eddington ratio of $L_{bol}/L_{Edd} = 0.2–0.5$.

NLS1 galaxies have been shown to have higher Eddington ratios on average than their Seyfert 1 counterparts, usually with $L/L_{Edd} \approx 1$ for NLS1 galaxies compared to $L/L_{Edd} \approx 0.1$ for a normal Seyfert 1 (Xu et al. 2007). However, there are a few objects, e.g., NGC 4395, that strongly contradict this dichotomy. Despite nearly identical spectra in the optical, POX 52 has an Eddington ratio that is more than 2 orders of magnitude larger than the $L_{bol}/L_{Edd} = 10^{-3}$ for NGC 4395 (Peterson et al. 2005), demonstrating that there must be substantial differences between the central engines of these prototypical low-mass AGNs. An Eddington ratio of ~0.5 suggests that POX 52 is not as highly accreting as many NLS1 galaxies and may represent an intermediate object in the continuum between NLS1 and Seyfert 1 galaxies.

The unabsorbed spectral slope (Γ) of POX 52 remained relatively unchanged between X-ray observations, suggesting little change in the intrinsic continuum emission. Shemmer et al. (2006) studied the correlation between X-ray spectral slope and accretion rate (L_{bol}/L_{Edd}) for AGNs up to $z \approx 2$, increasing the luminosity range to more than 3 orders of magnitude, almost twice as large as previous studies (e.g., Porquet et al. 2004; Wang et al. 2004; Bian 2005). Despite having a much lower mass than any of the sources used in the Shemmer et al. (2006) study ($M_{BH} \approx 10^7–10^{10} \, M_{\odot}$), POX 52 falls among the majority of objects in the sample when plotting Γ versus L_{bol}/L_{Edd}, making it consistent with this correlation, and suggests that this relationship is independent of black hole mass. With $\Gamma = 1.8$ and $L_{bol}/L_{Edd} \approx 0.2–0.5$, POX 52 falls in the overlapping region of the apparent distribution split between NLS1 ($\Gamma \approx 1.75–2.6$, $L_{bol}/L_{Edd} \approx 0.5–1.5$) and Seyfert 1 ($\Gamma \approx 1.5–2.3$, $L_{bol}/L_{Edd} \approx 0.05–0.5$) galaxies. It is important to note that bolometric luminosity is most often estimated from a single band using a bolometric correction (as done in Shemmer et al. 2006) and that there might be significantly more scatter or bias in these relations because of these corrections. However, since L_{bol} for POX 52 is calculated using a compilation of data sets over a wide range of wavelengths, it lends itself to a more secure calculation of the accretion luminosity of this object.

7.6. Black Hole–Host Galaxy Correlations

Relationships connecting the black hole mass with host galaxy properties, such as velocity dispersion, bulge mass, and bulge luminosity, can be useful in predicting the mass of a black hole of many objects from single photometric or spectroscopic observations. Determining the slope and amount of scatter in these correlations, specifically in the low-mass and high-mass ends of the black hole mass spectrum, can help us learn how black holes and host galaxies evolve together in time (e.g., Di Matteo et al. 2005).

If we extrapolate the M_{BH}-σ_* relation of Tremaine et al. (2002) down to $\sigma_* = 36$ km s^{-1} (Barth et al. 2004), we find a black hole mass of $M_{BH} = (1.4 \pm 1.1) \times 10^5 \, M_{\odot}$, which is consistent with the average black hole mass calculated from the mass estimators

described above. We use the F435W magnitude of the outermost Sérsic component in order to estimate an absolute B-band magnitude for the host galaxy of $M_B \approx -16.0$. Extrapolating the Marconi & Hunt (2003) M_{BH}-L_{bul} relation down to a lower luminosity, we find a predicted M_{BH} of $M_{BH} \approx 8.7 \times 10^5 \, M_{\odot}$, which is a factor of 2–5 higher than current estimates. The updated version of the Marconi & Hunt (2003) relation from Graham (2007) predicts a black hole mass of $M_{BH} \approx 7.4 \times 10^6 \, M_{\odot}$, which is a factor of 20–40 larger than estimated here.

The measured host galaxy color places a constraint on the age (and thereby mass-to-light ratio) of the galaxy stellar populations. The code kcorrect (Blanton & Roweis 2007) fits a combination of templates with a range of star formation histories, metallicities, and reddening values and returns the stellar mass (assuming a Chabrier [2003] initial mass function). Using either the HST measurements presented here or the BVRI measurements from Barth et al. (2004), we find a stellar mass of $M_{host} \approx 1.2 \times 10^9 \, M_{\odot}$. If we extrapolate the Häring & Rix (2004) M_{BH}-M_{bul} relation to the host galaxy mass of POX 52, the bulge mass implies a black hole mass of $M_{BH} \approx 1.1 \times 10^6 \, M_{\odot}$, a factor of 2–6 larger than our current estimate.

The compact systems investigated in Greene et al. (2008) follow the same trends. For the M_{BH}-L_{bul} relation, the black hole masses are on average 2 orders of magnitude less massive than their host galaxy luminosities would predict and are similarly an order of magnitude less massive than their host galaxy masses would predict. The divergent M_{BH}-M_{bul} and M_{BH}-L_{bul} relations in these galaxies as compared to elliptical galaxies may be an outcome of their different formation histories, as reflected in their different fundamental plane locations, which still leaves the possibility that the M_{BH}-σ_* relation represents a tighter empirical correlation in this low-mass regime. The M_{BH}-σ_* relation seems to more accurately reflect the properties of lower mass black holes and their host galaxies (Barth et al. 2005), whereas the M_{BH}-L_{bul} and M_{BH}-M_{bul} relations both overestimate the black hole mass by factors of ~2–100.

There has been recent work suggesting a correlation between black hole mass and Sérsic index for elliptical galaxies or the bulges of disk galaxies, for the purpose of predicting black hole masses in other objects (Graham & Driver 2007). The measured Sérsic index $n \approx 4$ and mass $M_{BH} \approx 3 \times 10^5 \, M_{\odot}$ make POX 52 a strong outlier in this relation, which previously only included objects with $M_{BH} \approx 10^6–10^9 \, M_{\odot}$. For $n = 4$, the mass predicted by this relation is $M_{BH} \approx 10^8 \, M_{\odot}$, approximately 3 orders of magnitude larger than all other mass estimates of POX 52 suggest. The inclusion of more objects like POX 52 and those in the GH sample demonstrates that there cannot be a single, tight M_{BH}-n correlation applicable across the entire mass spectrum of galaxies.

Recent HST imaging surveys have found evidence for a transition in the population of central star-cluster nuclei in early-type galaxies, such that galaxies more luminous than $M_B \approx -20.5$ mag, or more massive than a few times $10^{10} \, M_{\odot}$, tend to lack resolved central nuclei, while lower luminosity early-type galaxies are more likely to be nucleated (Wehner & Harris 2006; Ferrarese et al. 2006; Côté et al. 2006). These groups further found that the black holes in luminous ellipticals and the stellar nuclei in lower mass galaxies followed the same relationship between central object mass and host galaxy mass. They suggested that formation of a central massive object might be a universal property of early-type galaxies, but that the central object would be either a massive black hole or a central star cluster, depending on the host galaxy mass. It has already been demonstrated that NGC 4395 has both an AGN and a nuclear star cluster (Matthews et al. 1999),

and our GALFIT decompositions suggest the possibility that POX 52 might as well. Observations such as these provide further motivation to test for the presence of central black holes in dwarf ellipticals through dynamical searches or AGN surveys, and POX 52 is a unique object in this context, given its low stellar luminosity ($M_B = -16.0$ mag) and the unambiguous presence of a central black hole.

8. SUMMARY AND CONCLUSIONS

New *HST* observations have confirmed POX 52 to be a dwarf elliptical galaxy, with a Sérsic index of $n \approx 4.3$, $r_e \approx 1.15$, and $M_I = -17.3$. These parameters, along with the previously measured stellar velocity dispersion from Barth et al. (2004), show POX 52 to reside near the dwarf elliptical family in the fundamental plane. POX 52 was the first AGN found to reside in a dwarf elliptical galaxy, but more recent studies of low-mass AGNs and their host galaxies have found a number of similar objects (Greene et al. 2008).

We see strong variability over 500–10^4 s timescales with both *Chandra* and *XMM-Newton* and a substantial change in the absorbing column density due to partial covering over a 9 month time period. Data from the OM on *XMM-Newton* showed no significant variability in the UV over short $\sim 10^3$–10^5 s timescales. We see no variability within the $2\,\sigma$ errors in the 7 month period between the OM and *GALEX* NUV observations, but this does allow variations of 10%–35% on the $1\,\sigma$ uncertainty level. The *Spitzer* spectrum shows evidence of possible star formation due to the PAH features and red continuum, but that analysis is deferred to a later paper.

Including data from the VLA, *Spitzer*, *GALEX*, and 2MASS, we compile an extensive SED that shows POX 52 to be consistent with the radio-quiet template of more massive quasars and estimate a bolometric luminosity of $L_{bol} = 1.3 \times 10^{43}$ ergs s^{-1} by incorporating all of the available data. Using a variety of mass estimators, we find a range of black hole mass $M_{BH} \approx (1.8$–$4.2) \times 10^5$ $M_\odot$. We find that we are unable to determine the break frequency from the *Chandra* PSD, due to either a low signal-to-noise ratio or insufficient temporal sampling. If $\nu_B \approx 10^{-4}$ Hz, then our mass estimate from the X-ray excess variance of $M_{BH} = (3.9 \pm 1.7) \times 10^5$ $M_\odot$ is consistent with the optical mass estimates. Otherwise, new X-ray observations of POX 52 in an unabsorbed state with the larger effective area of *XMM-Newton* would be needed in order to determine ν_B and estimate the black hole mass with this method.

We have shown POX 52 to have an SED consistent with a scaled-down version of more massive type 1 quasars and that it is in a different accretion state than NGC 4395, as seen in the 2 orders of magnitude disparity between Eddington ratios. The number of low-mass AGNs known is increasing with new results from large AGN surveys, such as Greene & Ho (2004, 2007b), but POX 52 remains unique in that it is one of the nearest and best studied of the low-mass AGNs.

REFERENCES

Barth, A. J., Greene, J. E., & Ho, L. C. 2005, ApJ, 619, L151
Barth, A. J., Ho, L. C., Rutledge, R. E., & Sargent, W. L. W. 2004, ApJ, 607, 90
Bender, R., Burstein, D., & Faber, S. M. 1992, ApJ, 399, 462
Bentz, M. C., Peterson, B. M., Pogge, R. W., Vestergaard, M., & Onken, C. A. 2006, ApJ, 644, 133
Bian, W.-H. 2005, Chinese J. Astron. Astrophys. Suppl., 5, 289
Binggeli, B., & Jerjen, H. 1998, A&A, 333, 17
Blanton, M. R., & Roweis, S. 2007, AJ, 133, 734
Boller, T., Brandt, W. N., & Fink, H. 1996, A&A, 305, 53
Boller, T., Tanaka, Y., Fabian, A., Brandt, W. N., Gallo, L., Anabuki, N., Haba, Y., & Vaughan, S. 2003, MNRAS, 343, L89
Boselli, A., et al. 2005, ApJ, 629, L29
Buchanan, C. L., Gallimore, J. F., O'Dea, C. P., Baum, S. A., Axon, D. J., Robinson, A., Elitzur, M., & Elvis, M. 2006, AJ, 132, 401
Burstein, D., Bender, R., Faber, S., & Nolthenius, R. 1997, AJ, 114, 1365
Cardelli, J. A., Clayton, G. C., & Mathis, J. S. 1989, ApJ, 345, 245
Cash, W. 1979, ApJ, 228, 939
Chabrier, G. 2003, ApJ, 586, L133
Côté, P., et al. 2006, ApJS, 165, 57

Crummy, J., Fabian, A. C., Gallo, L., & Ross, R. R. 2006, MNRAS, 365, 1067
Debattista, V. P., Ferreras, I., Pasquali, A., Seth, A., De Rijcke, S., & Morelli, L. 2006, ApJ, 651, L97
Dickey, J. M., & Lockman, F. J. 1990, ARA&A, 28, 215
Di Matteo, T., Springel, V., & Hernquist, L. 2005, Nature, 433, 604
Dong, X., et al. 2007, ApJ, 657, 700
Elvis, M., et al. 1994, ApJS, 95, 1
Ferrarese, L., & Ford, H. 2005, Space Sci. Rev., 116, 523
Ferrarese, L., et al. 2006, ApJ, 644, L21
Filippenko, A. V., & Ho, L. C. 2003, ApJ, 588, L13
Filippenko, A. V., Ho, L. C., & Sargent, W. L. W. 1993, ApJ, 410, L75
Filippenko, A. V., & Sargent, W. L. W. 1989, ApJ, 342, L11
Fukugita, M., Shimasaku, K., & Ichikawa, T. 1995, PASP, 107, 945
Gallo, L. C., Boller, T., Tanaka, Y., Fabian, A. C., Brandt, W. N., Welsh, W. F., Anabuki, N., & Haba, Y. 2004a, MNRAS, 347, 269
Gallo, L. C., Tanaka, Y., Boller, T., Fabian, A. C., Vaughan, S., & Brandt, W. N. 2004b, MNRAS, 353, 1064
Gavazzi, G., Donati, A., Cucciati, O., Sabatini, S., Boselli, A., Davies, J., & Zibetti, S. 2005, A&A, 430, 411

Geha, M., Guhathakurta, P., & van der Marel, R. P. 2002, AJ, 124, 3073
———. 2003, AJ, 126, 1794
Graham, A. W. 2007, MNRAS, 379, 711
Graham, A. W., & Driver, S. P. 2007, ApJ, 655, 77
Greene, J. E., & Ho, L. C. 2004, ApJ, 610, 722
———. 2007a, ApJ, 656, 84
———. 2007b, ApJ, 670, 92
Greene, J. E., Ho, L. C., & Barth, A. J. 2008, ApJ, submitted
Greene, J. E., Ho, L. C., & Ulvestad, J. S. 2006, ApJ, 636, 56
Greisen, E. W. 2003, in Information Handling in Astronomy—Historical Vistas, ed. A. Heck (Dordrecht: Kluwer), 109
Grupe, D., Komossa, S., & Gallo, L. C. 2007, ApJ, 668, L111
Grupe, D., Leighly, K. M., Burwitz, V., Predehl, P., & Mathur, S. 2004a, AJ, 128, 1524
Grupe, D., Mathur, S., & Komossa, S. 2004b, AJ, 127, 3161
Hao, L., Weedman, D. W., Spoon, H. W. W., Marshall, J. A., Levenson, N. A., Elitzur, M., & Houck, J. R. 2007, in ASP Conf. Ser. 373, The Central Engine of Active Galactic Nuclei, ed. L. C. Ho & J.-M. Wang (San Francisco: ASP), 574
Häring, N., & Rix, H.-W. 2004, ApJ, 604, L89
Houck, J. R., et al. 2004, ApJS, 154, 18
Iwasawa, K., Fabian, A. C., Almaini, O., Lira, P., Lawrence, A., Hayashida, K., & Inoue, H. 2000, MNRAS, 318, 879
James, P. A. 1994, MNRAS, 269, 176
Jiang, P., Wang, J.-X., & Wang, T.-G. 2007, in ASP Conf. Ser. 373, The Central Engine of Active Galactic Nuclei, ed. L. C. Ho & J.-M. Wang (San Francisco: ASP), 143
Kalberla, P. M. W., Burton, W. B., Hartmann, D., Arnal, E. M., Bajaja, E., Morras, R., & Pöppel, W. G. L. 2005, A&A, 440, 775
Kaspi, S., Smith, P. S., Netzer, H., Maoz, D., Jannuzi, B. T., & Giveon, U. 2000, ApJ, 533, 631
Kellermann, K. I., Sramek, R., Schmidt, M., Shaffer, D. B., & Green, R. 1989, AJ, 98, 1195
Kinney, A. L., Calzetti, D., Bohlin, R. C., McQuade, K., Storchi-Bergmann, T., & Schmitt, H. R. 1996, ApJ, 467, 38
Kormendy, J. 1985, ApJ, 295, 73
Krist, J. 1993, in ASP Conf. Ser. 52, Astronomical Data Analysis Software and Systems II, ed. R. J. Hanisch, R. J. V. Brissenden, & J. Barnes (San Francisco: ASP), 536
Kunth, D., Sargent, W. L. W., & Bothun, G. D. 1987, AJ, 93, 29
Leighly, K. M. 1999a, ApJS, 125, 297
———. 1999b, ApJS, 125, 317
Marconi, A., & Hunt, L. K. 2003, ApJ, 589, L21
Markowitz, A., et al. 2003, ApJ, 593, 96
Matković, A., & Guzmán, R. 2005, MNRAS, 362, 289
Matthews, L. D., et al. 1999, AJ, 118, 208
McGill, K. L., Woo, J.-H., Treu, T., & Malkan, M. A. 2008, ApJ, 673, 703
McHardy, I. M., Koerding, E., Knigge, C., Uttley, P., & Fender, R. P. 2006, Nature, 444, 730
McHardy, I. M., Papadakis, I. E., Uttley, P., Page, M. J., & Mason, K. O. 2004, MNRAS, 348, 783
Miniutti, G., Ponti, G., Greene, J. E., Ho, L. C., Fabian, A. C., & Iwasawa, K. 2008, MNRAS, submitted

Moran, E. C., Eracleous, M., Leighly, K. M., Chartas, G., Filippenko, A. V., Ho, L. C., & Blanco, P. R. 2005, AJ, 129, 2108
Moran, E. C., Filippenko, A. V., Ho, L. C., Shields, J. C., Belloni, T., Comastri, A., Snowden, S. L., & Sramek, R. A. 1999, PASP, 111, 801
Nandra, K., George, I. M., Mushotzky, R. F., Turner, T. J., & Yaqoob, T. 1997a, ApJ, 476, 70
———. 1997b, ApJ, 477, 602
Nandra, K., O'Neill, P. M., George, I. M., & Reeves, J. N. 2007, MNRAS, 382, 194
Nikołajuk, M., Czerny, B., Ziółkowski, J., & Gierliński, M. 2006, MNRAS, 370, 1534
Nikołajuk, M., Papadakis, I. E., & Czerny, B. 2004, MNRAS, 350, L26
O'Neill, P. M., et al. 2006, ApJ, 645, 160
Onken, C. A., Ferrarese, L., Merritt, D., Peterson, B. M., Pogge, R. W., Vestergaard, M., & Wandel, A. 2004, ApJ, 615, 645
Osterbrock, D. E., & Pogge, R. W. 1985, ApJ, 297, 166
Page, K. L., O'Brien, P. T., Reeves, J. N., & Turner, M. J. L. 2004, MNRAS, 347, 316
Papadakis, I. E. 2004, MNRAS, 348, 207
Peng, C. Y., Ho, L. C., Impey, C. D., & Rix, H.-W. 2002, AJ, 124, 266
Peterson, B. M., Wanders, I., Bertram, R., Hunley, J. F., Pogge, R. W., & Wagner, R. M. 1998, ApJ, 501, 82
Peterson, B. M., et al. 2004, ApJ, 613, 682
———. 2005, ApJ, 632, 799
Piconcelli, E., Jimenez-Bailón, E., Guainazzi, M., Schartel, N., Rodríguez-Pascual, P. M., & Santos-Lleó, M. 2005, A&A, 432, 15
Porquet, D., Reeves, J. N., O'Brien, P., & Brinkmann, W. 2004, A&A, 422, 85
Raymond, J. C., & Smith, B. W. 1977, ApJS, 35, 419
Schlegel, D. J., Finkbeiner, D. P., & Davis, M. 1998, ApJ, 500, 525
Schmidt, M., & Green, R. F. 1983, ApJ, 269, 352
Shemmer, O., Brandt, W. N., Netzer, H., Maiolino, R., & Kaspi, S. 2006, ApJ, 646, L29
Shih, D. C., Iwasawa, K., & Fabian, A. C. 2003, MNRAS, 341, 973
Sirianni, M., et al. 1998, Proc. SPIE, 3355, 608
Skrutskie, M. F., et al. 2006, AJ, 131, 1163
Steffen, A. T., Strateva, I., Brandt, W. N., Alexander, D. M., Koekemoer, A. M., Lehmer, B. D., Schneider, D. P., & Vignali, C. 2006, AJ, 131, 2826
Strateva, I. V., Brandt, W. N., Schneider, D. P., Vanden Berk, D. G., & Vignali, C. 2005, AJ, 130, 387
Tananbaum, H., et al. 1979, ApJ, 234, L9
Thim, F., Hoessel, J. G., Saha, A., Claver, J., Dolphin, A., & Tammann, G. A. 2004, AJ, 127, 2322
Thompson, A. R., Clark, B. G., Wade, C. M., & Napier, P. J. 1980, ApJS, 44, 151
Tremaine, S., et al. 2002, ApJ, 574, 740
Valluri, M., Ferrarese, L., Merritt, D., & Joseph, C. L. 2005, ApJ, 628, 137
Vestergaard, M., & Peterson, B. M. 2006, ApJ, 641, 689
Wang, J.-M., Watarai, K.-Y., & Mineshige, S. 2004, ApJ, 607, L107
Weedman, D. W., et al. 2005, ApJ, 633, 706
Wehner, E. H., & Harris, W. E. 2006, ApJ, 644, L17
Xu, D., Komossa, S., Zhou, H., Wang, T., & Wei, J. 2007, ApJ, 670, 60